

**Accepted manuscript**

As a service to our authors and readers, we are putting peer-reviewed accepted manuscripts (AM) online, in the Ahead of Print section of each journal web page, shortly after acceptance.

**Disclaimer**

The AM is yet to be copyedited and formatted in journal house style but can still be read and referenced by quoting its unique reference number, the digital object identifier (DOI). Once the AM has been typeset, an ‘uncorrected proof’ PDF will replace the ‘accepted manuscript’ PDF. These formatted articles may still be corrected by the authors. During the Production process, errors may be discovered which could affect the content, and all legal disclaimers that apply to the journal relate to these versions also.

**Version of record**

The final edited article will be published in PDF and HTML and will contain all author corrections and is considered the version of record. Authors wishing to reference an article published Ahead of Print should quote its DOI. When an issue becomes available, queuing Ahead of Print articles will move to that issue’s Table of Contents. When the article is published in a journal issue, the full reference should be cited in addition to the DOI.

**Submitted:** 14 March 2019

**Published online in ‘accepted manuscript’ format:** 22 July 2020

**Manuscript title:** Rocking response of structures with shallow foundations on thin  
liquefiable layers

**Authors:** Orestis Adamidis\* and S. P. Gopal Madabhushi<sup>†</sup>

**Affiliations:** \*Institute of Geotechnical Engineering (IGT), ETH Zurich, Zurich, Switzerland  
and <sup>†</sup>Schofield Centre, University of Cambridge, High Cross, UK

**Corresponding author:** Orestis Adamidis, Institute of Geotechnical Engineering (IGT),  
ETH Zurich, Stefano-Franscini-Platz 5, 8093 Zurich, Switzerland.

**E-mail:** orestis.adamidis@igt.baug.ethz.ch

## **Abstract**

In the event of earthquake-induced liquefaction, structures with shallow foundations can suffer excessive settlement and rotation. In this paper, the rotational response of structures with shallow foundations resting on liquefiable layers with thickness equal to or smaller than the width of the foundation is examined through a series of dynamic centrifuge experiments. Moment-rotation backbone curves are extracted and the corresponding evolution of rocking stiffness with increasing rotation is depicted, in normalised terms. The proposed stiffness attenuation relation can be used for simplified predictions of maximum and residual rotation using rotational spring and dashpot models. Two such examples are presented, one using an iterative, equivalent-linear rotational spring approximation, and one using Masing's rules for cyclic response, extended with Pyke's hypothesis.

**Keywords:** centrifuge modelling; liquefaction; soil/structure interaction

## Introduction

Post-earthquake reconnaissance shows that in the event of earthquake-induced liquefaction, buildings with shallow foundations can suffer excessive settlement and tilting (e.g. Bray *et al.*, 2004; Cubrinovski *et al.*, 2011; Yasuda *et al.*, 2012). Settlement has been extensively researched, with studies employing centrifuge modelling (e.g. Dashti *et al.*, 2010a; da Silva Marques *et al.*, 2014; Bertalot & Brennan, 2015; Adamidis & Madabhushi, 2018a) or numerical modelling (e.g. Karamitros *et al.*, 2013b,c; Karimi & Dashti, 2016; Ayoubi & Pak, 2017), and aiming either to elucidate the mechanisms that produce settlement (e.g. Dashti *et al.*, 2010b; Adamidis & Madabhushi, 2018a) or to estimate its magnitude (e.g. Liu & Dobry, 1997; Bertalot *et al.*, 2013; Bray & Macedo, 2017; Bullock *et al.*, 2019b). Tilting had not received equal attention until recently. Tokimatsu *et al.* (2019) identified the key parameters contributing to tilting, while Bullock *et al.* (2019a) proposed an empirical model that correlates ultimate settlement with residual tilt, and a semi-empirical probabilistic model that predicts peak transient and residual tilt. However, more work is needed to elucidate the moment-rotation response of such systems and to depict the evolution of rocking stiffness with increasing rotation.

Unlike for liquefiable layers, the moment-rotation response of shallow foundations on non-liquefiable soils has been extensively examined (e.g. Housner, 1963; Gazetas, 1983, 1991; Butterfield & Gottardi, 1994; Chatzigogos *et al.*, 2009; Anastasopoulos *et al.*, 2010; Kourkoulis *et al.*, 2012; Pelekis *et al.*, 2018). A few studies that focus on the rotational response of shallow foundations on dry sand using centrifuge modelling have been published (e.g. Gajan *et al.*, 2005; Gajan & Kutter, 2009; Kokkali *et al.*, 2014; Heron *et al.*, 2015). In these studies, moment-rotation backbone curves were calculated from experimental results, which capture the reduction of rotational stiffness with increasing rotation, due to soil softening and uplifting of the foundation. Gajan *et al.* (2005) and Kokkali *et al.* (2014) presented graphs of diminishing rocking stiffness with increasing rotation, while Heron *et al.* (2015) opted for the development of a macro-element that captures the moment-rotation response. Particularly valuable was the work of Gazetas *et al.* (2013), who presented dimensionless graphs for the degradation of rocking stiffness with increasing rotation, based on numerical simulations of shallow foundations resting on undrained clay layers. These graphs were subsequently used to develop simplified approximations with non-linear rotational springs by Anastasopoulos & Kontoroupi (2014) and equivalent-linear rotational springs by Adamidis *et al.* (2014), with the purpose of estimating maximum rotation.

In this paper, results from seven dynamic centrifuge experiments are presented, with the aim of examining the co-seismic rotational response of shallow foundations resting on liquefiable layers. The focus is on the moment-rotation response of systems where the structure responds by rocking. The degradation of rocking stiffness with increasing rotation is examined and meaningful ways of normalisation are proposed. A relation that captures the attenuation of normalised rocking stiffness with increasing normalised rotation is presented. Based on this relation, simplified rotational spring and dashpot approximations can be developed to estimate maximum transient and residual tilt. Two such examples are given, one using an iterative, equivalent-linear rotational spring approximation (e.g. Adamidis *et al.*, 2014), and one using a non-linear rotational spring approximation, based on the extension of Masing's rules (Masing, 1926) that was proposed by Pyke (1979). The performance of these approximations is assessed not only for the 10 seismic events involving rocking from the centrifuge test series presented here, but also for 70 additional seismic events extracted from four centrifuge tests performed at UC Davis and included in the FLIQ database (Allmond *et al.*, 2015).

## Experimental methods

The data used in this paper were recorded during seven dynamic centrifuge tests. Dynamic centrifuge modelling was chosen in order to accurately model the liquefaction process, the drainage conditions, and the interaction of the soil with the examined foundations. For a detailed outline of the advantages of centrifuge modelling for geotechnical research the reader is referred to Madabhushi (2014), where a full list of scaling laws for centrifuge modelling can also be found.

The centrifuge tests presented here were performed on the Turner Beam Centrifuge of the Schofield Centre, at the University of Cambridge. They all modelled the plane-strain problem of a strip foundation resting on a layer of fully-saturated liquefiable sand. The soil layers and the foundations remained submerged in pore fluid throughout the experiments. Sketches of the cross-sections of the models examined are shown in figure 1.

The applied centrifugal acceleration was  $50g$  at the level of the foundation. The width of all footings was  $B = 4.6$  m in prototype scale and the aspect ratio was constant for all structures, at  $h_{CM} / B = 0.58$ , with  $h_{CM}$  the height of the structure's centre of mass, measured from the base of the foundation. The depth of the liquefiable layer ( $D_L$ ) and the bearing pressure ( $q$ ) applied by the foundation were altered for each experiment, as detailed in table 1

The model container used was a rigid box. One side of the box included a polymethyl methacrylate window, through which a high frame-rate camera (MotionBLITZ EoSens mini2) could monitor a cross-section of the plane-strain model. Particle Image Velocimetry (PIV) was used to calculate displacement fields within the visible soil section and to monitor markers on the structure (White *et al.*, 2003). In order to limit the boundary effects that a rigid box introduces, a material called Duxseal was placed at the edges of the box, as shown in the sketches of figure 1. According to Steedman & Madabhushi (1991), Duxseal can absorb about 65% of incident wave energy for P and S waves. As discussed in Adamidis & Madabhushi (2018a), boundary effects are not expected to have been significant for the experiments where  $B / D_L \geq 1$ .

Hostun sand was used for the preparation of the sand layers (properties in table 2). The layers were prepared with air pluviation, using the automatic sand pourer of the Schofield Centre (Madabhushi *et al.*, 2006) and targeting a relative density of 40% for all tests, based on the values of  $e_{min}$  and  $e_{max}$  of table 2. The instrumentation used included miniature piezoelectric accelerometers (Acc), microelectromechanical system accelerometers (MEMS), pore pressure transducers (PPTs), and linear variable displacement transducers (LVDTs). The positioning of instruments is shown in figure 1.

An inconsistency exists between the scaling laws of dynamic and seepage time in centrifuge modelling (see, for instance, Madabhushi, 2014). In order to overcome it, viscosity scaling was performed, using a high viscosity aqueous solution of hydroxypropyl methylcellulose to saturate the model, prepared as described in Adamidis & Madabhushi (2015). Since the applied centrifugal acceleration was  $50g$ , the targeted viscosity of the solutions prepared was  $50mPas$ . Saturation was performed via the computer-controlled system described in Stringer & Madabhushi (2009). The process followed included three cycles of applying vacuum and flushing the model with  $CO_2$  prior to controlled saturation under vacuum.

Two structures, 'a' and 'b', were used throughout the series of experiments. Their sketches are given in figure 2, while table 1 lists which structure was used for each test. Their mass was adjusted using brass plates, in a way that maintained their aspect ratio ( $h_{CM} / B$ ) constant. The structures were made stiff, their fixed-base frequency higher than the frequency of the

imposed excitation, to promote a rigid-body response and thus simplify the problem. The friction angle at the interface between the structures and the sand was measured using direct shear test apparatus and was found to be  $\delta = 28.8^\circ$ . The structures were instrumented using MEMS accelerometers, positioned as shown in figure 2. An LVDT monitored the settlement at the centre of each structure (fig. 1) while markers on the foundation were used to track their movement using image analysis. The properties of the structures are outlined in table 3. The rotation of the foundations was calculated by combining image analysis, which tracked markers on the foundation, with accelerometer recordings. The low frequency component of rotation, which contributed to residual tilt, was calculated from PIV results, while the high frequency, ‘dynamic’ rotation was computed from the records of MEMS accelerometers. The imposed excitations were pseudo-harmonic, generated using the Stored Angular Momentum (SAM) actuator described by Madabhushi *et al.* (1998). The targeted frequency was  $1\text{ Hz}$  in prototype scale and the targeted duration was  $20\text{ s}$  in prototype scale. The amplitude of the input motions in prototype scale was about  $0.2\text{ g}$  for the first earthquake and  $0.3\text{ g}$  for the second earthquake.

More information about the experimental methods can be found in Adamidis (2017).

#### Structural response

In order to investigate whether the structures did indeed respond as rigid bodies, Fast Fourier Transforms (FFTs) for the input acceleration and the acceleration recorded at the top of each structure are plotted in figure 3. Large Fourier components were calculated at the same frequencies for both acceleration recordings presented for each test, indicating that the structure responded at the frequency of the input motion, with very little oscillation at any other frequency. The dominant frequency of the input motion was  $1\text{ Hz}$ , with a parasitic frequency generated by the actuator at  $3\text{ Hz}$ . In all cases, the frequencies excited by the input motion remained far from the fixed-base frequency of the structures, measured before and after the centrifuge experiments and included in the graphs of figure 3 as dotted lines labelled ‘f.b.f.’. The lack of any signs of flexural response within the structures allows the interpretation of results by assuming a rigid body response.

#### Rotational response

Conventions used in this paper regarding moment and rotation are graphically outlined in the sketch of figure 4. Settlement and moment refer to the centre of the base of the foundation and counter-clockwise rotation is considered positive. Based on these conventions, graphs of settlement versus rotation are presented in figure 5.

In all experiments with  $B/D_L \geq 1$ , a rocking response was established, with dynamic rotations of significant amplitude. In these experiments, an area of increased effective stress formed below the centre of the foundation, which reached the base of the liquefiable layer and transmitted sufficient acceleration to the structure for a rocking response to be established. This mechanism did not necessarily appear in deeper layers, leading to different types of rotational response. For instance, during the first earthquake of OA4, the amplitude of dynamic rotation reduced as the earthquake advanced. In this test, a deep liquefiable layer was combined with a light structure. Soil softening deep below the foundation limited the acceleration that reached the structure, thus reducing the amplitude of dynamic rotation and preventing a rocking response. In contrast, the heavier structure of OA5 led to the creation of a zone of higher effective stress beneath it, which allowed increased accelerations to reach the structure. As a result, the dynamic rotational amplitude in OA5 increased as the first earthquake advanced. During the second earthquake of OA4 and OA5, the increased

embedment of the foundations led to a response that was closer to rocking, especially for the heavier structure of OA5. Overall, for the deep layers examined, the rotational response established depended significantly on the combination of bearing pressure and embedment of the structure. Though not altered in this investigation, the aspect ratio should also be expected to be of importance. Since the focus of this paper is the rocking response of shallow foundations on liquefiable soil, only thin layers with  $B/D_L \geq 1$  are considered from now on. In all such cases examined, structures responded with rocking. A more detailed discussion on the mechanisms that develop below shallow foundations on liquefiable layers of different depths can be found in Adamidis & Madabhushi (2018a).

Moment ( $M$ ) was calculated at the base of the centre of the foundation, as outlined in equation 1. The acceleration at the centre of mass of the structure ( $a_{CM}$ ) was computed using the recordings of the MEMS accelerometers mounted on the structure (fig. 2), assuming a rigid body response. In equation 1,  $m$  is the mass of the structure,  $h_{CM}$  is the height of the centre of mass, measured from the base of the foundation,  $I_{CM}$  is the mass moment of inertia around the centre of mass, and  $a_{CM_x}$  is the horizontal component of acceleration at the centre of mass of the structure, in coordinates local to the structure. Acceleration  $a_{CM_x}$  was calculated using MEMS recordings, which capture both dynamic and centrifugal acceleration.

$$M = -I_{CM} \ddot{\theta} + a_{CM_x} m h_{CM} \quad (1)$$

Using equation 1, moment-rotation loops were calculated, as shown in the graphs of figure 6. The rotation ( $\theta$ ) depicted in figure 6 refers to the inclination of the structure and includes dynamic and residual rotation. In all cases, residual rotation was gradually accumulated as the earthquake advanced. Moment was normalised by  $BV/2$ , where  $B$  is the width of the foundation and  $V$  is the weight of the structure.  $BV/2$  is the moment that would be required to rotate the structure around its edge if it were resting on a rigid base. This normalisation was quite successful in matching the levels of maximum normalised moment reached at large rotational angles by structures of different weight that responded by rocking.

#### Rocking stiffness calculation

##### Spring and dashpot model

Assuming a simplified rotational spring and dashpot model at the base of the foundation, with  $K_R$  as the stiffness coefficient and  $C_R$  as the dashpot coefficient, the following expression applies, if  $M$  is the moment:

$$M = K_R \theta + C_R \dot{\theta} \quad (2)$$

The above expression implies no coupling between the horizontal and rotational motion, a common assumption in studies examining the dynamic rocking of shallow foundations in a centrifuge (e.g Gajan *et al.*, 2005; Heron *et al.*, 2015), which is necessary to derive results regarding stiffness with the available experimental data. Though a simplification of reality, this assumption is reasonable for the shallow foundations examined here, which initially rested on the soil surface and did not get significantly embedded in the soil during the earthquakes.

Expressing the dashpot coefficient as a function of damping ratio  $\xi$ :

$$C_R = \frac{2K_R \xi}{\omega} \quad (3)$$

Considering the pseudo-harmonic nature of the applied input motion, it would be reasonable to simplistically assume the following expression, with  $\omega$  the radial velocity:

$$\theta = \theta_{max} \sin(\omega t) \quad (4)$$

Using equations 3 and 4, equation 2 is written as follows:

$$\frac{M}{\theta_{max}} = K_R \left( \sqrt{1 + (2\xi)^2} \right) \sin(\omega t + \phi_M) \quad (5)$$

$$\text{with } \phi_M = \tan^{-1}(2\xi) \quad (6)$$

Based on equation 5, the moment at the point of maximum rotation within a loop can be used to calculate rocking stiffness, as long as the damping ratio is known:

$$K_R = \frac{M_{\theta_{max}}}{\theta_{max} \sqrt{1 + (2\xi)^2}} \quad (7)$$

It should be pointed out that this approach would be most appropriate for moment-rotation loops that are symmetrical in terms of rotation. However, in the experimentally recorded loops, rotation was accumulated in one direction through consecutive loading cycles. This accumulation of rotation had to be taken into account to appropriately depict the evolution of secant rocking stiffness and to produce moment-rotation backbone curves that corresponded well to the experimental results. For this reason, the value of  $\theta_{max}$  used included accumulated rotation. Considering that in all experiments the structure gradually tilted in one direction, only the rotational half-cycles corresponding to the direction of accumulated rotation were chosen for secant stiffness calculation. The only calculation for which accumulated tilt was excluded was that related to dissipated energy, using the area enclosed within moment-rotation loops, so as to produce closed loops. Thus, the results obtained correspond to a symmetrical moment-rotation loop of rotational amplitude  $\theta_{max}$ , where the same amount of energy is dissipated as in the non-symmetrical loop of the experiment. This approach was chosen to generate results appropriate for simplified rotational spring approximations.

#### Damping ratio

Damping ratio was calculated both using the phase lag between moment and rotation (eq. 6) and using the area contained within moment-rotation loops. Area was calculated for each half-cycle, as outlined in figure 7, only considering dynamic rotation that excludes accumulated tilt. Both methods of damping ratio calculation, i.e. using phase lag or loop area, yielded similar results regarding stiffness. However, the method using loop area produced reduced scatter in damping ratio and was thus deemed preferential.

The values of damping ratio calculated are shown in figure 8a versus dynamic rotation amplitude, using dynamic rotation for the calculation of elastic area. High values of damping ratio, up to 60% were calculated for small dynamic rotations. As the amplitude of dynamic rotation increased, the damping ratio decreased to values of about 20%. The same trend was followed by all rocking foundations, irrespective of the weight of the structure or the depth of the layer that liquefied. A curve was fitted to the available data points, as follows:

$$\xi_{dyn}(\%) = 60 \exp(-400\theta_{dyn}) + 20 \quad (8)$$

This fit was based on available experimental points and should be used with caution at very small amplitudes of dynamic rotation, for which it gives large values of damping ratio. The trend of reducing damping ratio with increasing rotation seems counter-intuitive if one has hysteretic damping in mind, where damping ratio typically increases with increasing rotational amplitude. Further investigation is required regarding this response. Damping ratio could be related to the extent of the mobilised mechanism, which reduces as the earthquake



advances. It is worth pointing out that the trend of reducing damping ratio with increasing rotation has been reported before in dynamic centrifuge testing of rocking structures, albeit for non-liquefiable soil layers, by Kokkali *et al.* (2014).

In figure 8b, an equivalent damping ratio is presented, which corresponds to the maximum rotation recorded for each half-cycle, including the accumulated tilt. Maximum rotation including accumulated tilt was used to calculate the elastic area. The calculated damping ratio corresponds to a symmetrical cycle of rotational amplitude equal to the maximum rotation used, which dissipates the same energy as that of the experimental cycle. A curve was fitted to these data points, as follows:

$$\xi(\%) = 60 \exp(-200\theta) + 5 \quad (9)$$

#### Shear modulus and frequency dependence

Before secant rocking stiffness is calculated, one more consideration needs to be addressed, regarding the frequency dependence of rocking stiffness. As the frequency of the rocking motion increases, the observed rotational stiffness decreases from its ‘static’ value, a phenomenon studied extensively for machine foundations (Gazetas, 1983). The reduction of rocking stiffness from its ‘static’ value can be evaluated based on the dimensionless frequency parameter  $\alpha_0 = \frac{\omega B}{2V_s}$ , where  $V_s$  is the shear velocity of the soil. Shear velocity  $V_s$

estimations can be made using the shear modulus  $G$ .

An expression describing the small-strain shear modulus  $G_{max}$  of Hostun sand was proposed by Azeiteiro *et al.* (2017), based on bender element measurements:

$$G_{max} = 293 p'_{ref} f(e) \left( \frac{p'}{p'_{ref}} \right)^{0.49} \quad (10)$$

where  $p'_{ref}$  is the atmospheric pressure and  $f(e)$  is a function of void ratio, following Hardin & Drnevich (1972):

$$f(e) = \frac{(2.97 - e)^2}{1 + e} \quad (11)$$

In terms of shear modulus degradation with increasing shear strain, the relation proposed by Ishibashi & Zhang (1993) can be used:

$$\frac{G}{G_{max}} = K_{(\gamma)} (p')^{(m(\gamma) - m_0)} \quad (12)$$

Where  $K_{(\gamma)}$  and  $(m(\gamma) - m_0)$  are calculated as follows:

$$K_{(\gamma)} = 0.5 \left[ 1 + \tanh \left[ \ln \left( \frac{0.000102}{\gamma} \right)^{0.492} \right] \right] \quad (13)$$

$$(m(\gamma) - m_0) = 0.272 \left[ 1 - \tanh \left[ \ln \left( \frac{0.000556}{\gamma} \right)^{0.4} \right] \right] \quad (14)$$

Damping ratio can also be estimated following Ishibashi & Zhang (1993):

$$\xi = 0.333 \left[ 0.586 \left( \frac{G}{G_{max}} \right)^2 - 1.547 \left( \frac{G}{G_{max}} \right) + 1 \right] \quad (15)$$

In order to verify that the above expressions are appropriate for the layers of dry-pluviated Hostun sand examined in the centrifuge, results from two instrumented soil columns were used. These soil columns were included in centrifuge tests OA2 and OA3, a sketch of which is shown in figure 9. These tests included layers of fully saturated Hostun sand, prepared in exactly the same way as the layers of tests OA4 to OA12, having the same relative density and being saturated with viscous pore fluid of the same viscosity. The instrumented soil columns used were included in the left half of the models shown in figure 9. In the right half, a flexible but impermeable chamber was included, meant to assess the importance of drainage during earthquake-induced liquefaction, as described in Adamidis & Madabhushi (2018b). Results from these tests were used here for the estimation of shear modulus because they corresponded to the response of a free-field. In tests OA4 to OA12 discussed in this paper, large shear mechanisms were developed due to the presence of a structure, which reached the edges of the available soil, so that a true free-field response was not obtained even close to the boundaries of the box (Adamidis & Madabhushi, 2018a).

Within the instrumented free-field soil columns of tests OA2 and OA3, one-dimensional wave propagation was assumed. Time histories of shear stress  $\tau$  and shear strain  $\gamma$  were calculated, using acceleration measurements and following the methodology proposed by Elgamal *et al.* (1996). Special care was given to filtering, as suggested by Brennan *et al.* (2005). Results of produced  $\tau - \gamma$  loops were presented in Adamidis & Madabhushi (2018b).

The comparison of experimentally calculated values for  $G$  from tests OA2 and OA3 with idealised shear modulus degradation using the expressions proposed by Azeiteiro *et al.* (2017) and Ishibashi & Zhang (1993) is shown in figure 10. Mean effective stress  $p'$  was calculated for each point, using experimental measurements of excess pore pressure and making the assumption that  $K' = \frac{\sigma'_h}{\sigma'_v}$  varied linearly as a function of excess pore pressure

ratio  $r_u$ , with  $K' = 1 - \sin(\phi')$  when  $r_u = 0$  and  $K' = 1$  when  $r_u = 1$ . Though lateral stresses are difficult to measure, data from direct simple shear tests and DEM simulations support the assumption made (Youd & Craven, 1975; Dabbeet *et al.*, 2012). Using the calculated value of  $p'$  for each point,  $(m(\gamma) - m_0)$  was computed, following expression 14. Then,  $K(\gamma)$  was calculated, following equation 12 and taking  $G_{max}$  from equation 10. In terms of damping ratio, two lines were plotted on top of the experimentally calculated values in figure 10b, for  $p' = 1 \text{ kPa}$  and for  $p' = 10 \text{ kPa}$ . These lines represent a reasonable range for the soil columns examined, which reached full liquefaction. While slightly overestimating degradation of  $G$  compared to the experimental points, likely due to an overestimation of  $G_{max}$ , the comparison was deemed adequate to adopt the formulations of Azeiteiro *et al.* (2017) for  $G_{max}$  and Ishibashi & Zhang (1993) for the evolution of  $G$  and  $\xi$  with increasing strain for the Hostun sand layers that are of interest in this paper.

With expressions describing the shear modulus  $G$  of the soil in place, conservative estimations about shear wave velocity  $V_s$  were made, in order to assess the effect of frequency on rocking stiffness. Initially, a relevant value of  $G_{max}$  is necessary. Knowing the void ratio, a value of  $p'$  can be calculated, taking into account measured excess pore water pressures. Figure 11 shows measurements of excess pore water pressure under the right edge of all foundations. Conservatively, a value of  $\Delta U \approx 20 \text{ kPa}$  can be taken for layers with

$B/D_L \geq 1$ . Also, the lightest structure examined is considered. Defining  $K' = \frac{\sigma'_h}{\sigma'_v}$  as a linear function of  $r_u$ , as described in the previous paragraph, in the worst case  $p' \approx 25 \text{ kPa}$ . For this value, equation 10 gives  $G_{max} \approx 40 \text{ MPa}$ . Figure 12 presents time histories of shear strain under the foundation, calculated using results from image analysis. Conservatively assuming a level of shear strain per cycle of  $\gamma \approx 3\%$ , equation 12 gives a value of  $G \approx 0.9 \text{ MPa}$ , for which  $V_s \approx 25 \text{ m/s}$ . Thus, values of  $\alpha_0 < 0.6$  are expected to be of interest. At worst, frequency effects could reduce rocking stiffness by about 10%, assuming an elastic halfspace as in Gazetas (1991). In the centrifuge tests presented here, this effect would be less significant due to the non-linear soil response. As a result, reductions in rocking stiffness due to frequency effects were assumed to be sufficiently low to be neglected.

#### Calculated rocking stiffness

The values of secant rocking stiffness calculated based on equation 7 are concentrated in figure 13. Experiments with  $B/D_L \geq 1$  are included. As also seen in centrifuge experiments with non-liquefiable soils (e.g Gajan *et al.*, 2005; Kokkali *et al.*, 2014), rocking stiffness decreases with increasing rotation. As one would have expected, lower values of rocking stiffness correspond to the lighter structure, which imposed lower bearing pressure, leading to a reduced shear modulus in the soil. The effects of the depth of the liquefied soil are not easily identifiable. It seems that as long as a rocking response is established, the bearing pressure applied by the structure is more significant for rocking stiffness than the depth of the layer that has liquefied. The pairs of moment-rotation that correspond to the calculated values of secant rocking stiffness are shown as points plotted over the moment-rotation loops of figure 6.

#### Normalisation of rocking stiffness and rotation angle

##### Normalisation framework

The expression of the calculated values of secant rocking stiffness of figure 13 in normalised terms can significantly increase their value for use in simplified, rotational spring methodologies for the estimation of maximum rotation during a seismic event. Gazetas *et al.* (2013) presented a framework for the normalisation of secant rocking stiffness of shallow foundations, resting on layers of undrained clay.

According to this framework, the secant rocking stiffness  $K_R$ , normalised with the elastic rocking stiffness  $K_{R,el}$  is a function of rotation  $\theta$  and factor of safety versus vertical load  $F_s$ , given a unique curve for the degradation of  $\frac{G}{G_{max}}$  with increasing shear strain  $\gamma$ . In the case

of sands, the normalised shear modulus degradation curve proposed by Ishibashi & Zhang (1993) can be used, as was done in this paper. As a result, one could expect for the problem studied here:

$$\frac{K_R}{K_{R,el}} = f(\theta, F_s) \quad (16)$$

Gazetas *et al.* (2013) succeeded in presenting the rocking stiffness  $K_R$  as the product of elastic rocking stiffness  $K_{R,el}$ , diminished using a function of the factor of safety versus vertical load that takes into account initial yielding within the soil ( $\psi(F_s)$ ), times a

degradation function  $\chi\left(\frac{\theta}{\theta_s}, F_s\right)$ , which depicts the decrease of normalised rocking stiffness with increasing rotation, normalised with a reference rotation  $\theta_s$ , and also depending on the factor of safety versus vertical load:

$$K_R = K_{R,el} \cdot \psi(F_s) \cdot \chi\left(\frac{\theta}{\theta_s}, F_s\right) \quad (17)$$

In an effort to examine the applicability of such a normalisation here, values for elastic rocking stiffness  $K_{R,el}$ , reference rotation  $\theta_s$ , and factor of safety versus vertical load  $F_s$  must be estimated.

Initial rocking stiffness and reference rotation

Initially, the elastic rocking stiffness,  $K_{R,el}$ , must be calculated. Instead of using the expression in Gazetas *et al.* (2013) for the rocking stiffness of a strip foundation on an elastic halfspace, the equation suggested by Gazetas (1983), based on Jakub & Roesset (1977a,b), and which accounts for embedment ( $Emb$ ) and for the presence of a rigid base below the examined layer was employed, as more appropriate for the experiments studied here. This estimation is as follows, with  $\nu$  being Poisson's ratio:

$$K_{R,el} = \frac{\pi G \left(\frac{B}{2}\right)^2}{2(1-\nu)} \left(1 + \frac{B}{10D_L}\right) \left(1 + \frac{2Emb}{B}\right) \left(1 + \frac{2Emb}{3D_L}\right) \quad (18)$$

Using the elastic rocking stiffness  $K_{R,el}$ , a reference rotation  $\theta_{s,el}$  can be calculated, which is close to the rotation at which a strip foundation uplifts if elasticity is assumed:

$$\theta_{s,el} = \frac{VB}{4K_{R,el}} \quad (19)$$

Gazetas *et al.* (2013) proposed a function  $\psi(F_s)$  that accounts for initial yielding within the soil to reduce  $K_{R,el}$ , based on the factor of safety versus vertical load  $F_s$ . Using this function, the rocking stiffness of surface foundations at vanishingly small rotations  $K_{R,0}$  was proposed as:

$$K_{R,0} \approx K_{R,el} \psi(F_s) = K_{R,el} \left(1 - \frac{0.8}{F_s}\right) \quad (20)$$

Using this expression for initial rocking stiffness  $K_{R,0}$ , a reference rotation  $\theta_s$  was also proposed:

$$\theta_s = \frac{VB}{4K_{R,0}} \quad (21)$$

Factor of safety versus vertical load

Multiple methodologies are available for the calculation of the ultimate vertical load that can be taken up by a strip foundation. Following most methods, for the case of a vertically and centrally loaded strip foundation resting on saturated sand, the ultimate load would be calculated using an equation as the following, if  $q_f$  is the ultimate load,  $q'_{over}$  is the effective stress due to overburden soil, and  $\gamma'_s$  is the buoyant unit weight of the soil:

$$q_f = q'_{over} N_q + \frac{1}{2} \gamma'_s B N_\gamma \quad (22)$$

The factors  $N_q$  and  $N_\gamma$  are typically given by graphs or equations, according to the methodology used. However, when calculating the ultimate load for foundations in the centrifuge tests performed, the limited depth of the layers must also be taken into account. According to DIN 4017, the depth of the soil layer must be more than  $1.7B$  for the methodology to apply. As a result, one should not use typical methodologies for the shallow layers that are of interest here.

The ultimate load that can be taken up by strip foundations resting on thin soil layers was studied by Mandel & Salençon (1972), who offered modifications for  $N_q$  and  $N_\gamma$  that account for reduced layer thickness. The values they calculated assumed the presence of a rough, rigid base for the layers, an assumption fitting for the layers examined in the centrifuge, which rested on a thick metal plate overlaid with a thin, rough, porous sheet. Moreover, they assumed a rough interface at the foundation. The foundations used in the centrifuge tests consisted of metal plates and the angle of friction between them and the sand was  $\delta \approx 29^\circ$ . While the assumption of a rough interface at the foundation does not perfectly correspond to the interface of the examined foundations, the results are not expected to be particularly sensitive to the roughness of the footing (Andrawes *et al.*, 1996).

The values of  $N_q$  and  $N_\gamma$  proposed by Mandel & Salençon (1972) were used to calculate the factor of safety versus vertical load at the beginning of each test as shown in table 4. Any embedment of the foundations developed before the first earthquake was also taken into account. Expectedly, as the layers became more shallow, the initial safety factors versus vertical loading increased significantly.

The process outlined here was also the basis for further calculations, regarding the factors of safety versus vertical load during seismic shaking, as excess pore pressures were generated. The calculation process for each half-cycle is detailed below.

#### Calculation process

To implement a normalisation on the points of figure 13, one has to calculate values for initial rocking stiffness  $K_R$ , reference rotation  $\theta_s$ , and factor of safety versus vertical load  $F_s$ . However, these values are dependent on the level of embedment of the foundation and on the density of the soil, as well as on the level of effective stress, and thus on the generation of excess pore water pressure. Foundation embedment and soil density both change as the earthquake advances, while excess pore water pressure changes not only in time but also in space.

Foundation embedment was calculated for each half-cycle corresponding to the points of figure 13, based on results from image analysis. It was found that the embedment could also be estimated from the difference of settlement at the centre of the structure from that measured at the free field, with results not substantially different from those stemming from image analysis. Moreover, the initial value of void ratio for the soil layer was updated for each half-cycle, based on the free-field settlement measurement and assuming one-dimensional compression. This change was not particularly significant during an earthquake. It should be pointed out that one should not expect significant densification under a foundation that rests on a liquefiable layer during an earthquake. The settlement produced is mostly due to shear strains, while soil close to the foundation even dilates due to excessive shearing (see the shear and volumetric strain contours of Adamidis & Madabhushi (2018a)). Subsequently, excess pore water pressure generation was targeted. A location at which excess

pore water pressure should be considered was chosen. Looking at the contours of shear strains during a typical rotational half-cycle in figure 14, one can notice that for systems where  $B/D_L \geq 1$ , the shear mechanism produced affects primarily the soil under the edges of the foundation and is limited to shallow depths. As a result, the shallowest pore pressure transducers, placed at about  $0.2B$  under the edges of the foundation were used. Their results are shown in figure 11. Using these time histories, an average value of excess pore pressure was calculated for each half-cycle, for the time between the instants of maximum moment and rotation.

Using the above estimations, mean effective stress  $p'$  under the edge of the foundation was calculated for each half-cycle. This value was in turn used to compute the small-strain shear modulus,  $G_{max}$ , following equation 10. Knowing  $G_{max}$  and current embedment, the elastic rotational stiffness  $K_{R,el}$  was calculated from equation 18. Poisson's ratio was taken as  $\nu \approx 0.3$ . This value, appropriate for drained conditions, was preferred to  $\nu = 0.5$  that one might assume for undrained loading. As inferred from the excess pore water pressures of figure 11, soil under the foundation was not liquefied and even for liquefied soil, the undrained assumption is not realistic within the time-frame of an earthquake (Adamidis & Madabhushi, 2018b). Based on  $K_{R,el}$ , reference rotation  $\theta_{S,el}$  was calculated from equation 19. The factor of safety versus vertical loading  $F_s$  was computed for each half-cycle, using equation 22, taking into account embedment, and with factors  $N_q$  and  $N_\gamma$  as given by Mandel & Salençon (1972). In order to lower the factor of safety as excess pore water pressure was generated, the measured value of excess pore water pressure was used to artificially reduce the unit weight of sand, taken as:  $\gamma'_s = \frac{\sigma'_z}{z}$ .

#### Normalised rocking stiffness degradation

Following the process described above, a value of  $K_{R,el}$  and  $\theta_{S,el}$  was calculated for each half-cycle considered for the points of figure 13. The outcome of normalisation using  $K_{R,el}$  and  $\theta_{S,el}$  is shown in figure 15. Following normalisation, a unique curve was formed. A function is proposed, which describes the evolution of normalised stiffness given normalised rotation, and which reasonably captures the experimental results:

$$a = 0.2 \quad (23)$$

$$b = 0.8 \quad (24)$$

$$c = 0.8 \quad (25)$$

$$\frac{K_R}{K_{R,el}} = \left( 1 - \left( 1 - \frac{1}{a} \right) \left( \frac{\theta}{\theta_{S,el}} \right)^{\frac{b}{(c+1)(a+1)}} \right)^{-1}, \frac{\theta}{\theta_{S,el}} \leq 1 \quad (26)$$

$$\frac{K_R}{K_{R,el}} = a \left( \frac{c+1}{c + \frac{\theta}{\theta_{S,el}}} \right)^b, \frac{\theta}{\theta_{S,el}} > 1 \quad (27)$$

The proposed stiffness degradation relation is shown as a black curve in figure 15. A definition for normalised stiffness in the case of  $\frac{\theta}{\theta_s} \leq 1$  is proposed (eq. 26), despite the lack of experimental data in this range of normalised rotation, for the sake of completeness and so that full moment-rotation backbone curves can be calculated. Equation 26 takes a value of 1 for zero rotation and a value of  $a$  for  $\frac{\theta}{\theta_s} = 1$ , so that it matches equation 27 at  $\frac{\theta}{\theta_s} = 1$ . Its

formulation also ensures that it has the same slope as equation 27 at  $\frac{\theta}{\theta_s} = 1$  in the graph of figure 15.

Considering the success of normalisation using elastic parameters, further efforts for normalisation using  $K_{R,0}$  and  $\theta_s$ , which take into account the factor of safety versus vertical load, were not pursued. However, it is worth examining why the significant dependence on the factor of safety versus vertical loading that was reported by Gazetas *et al.* (2013) for shallow foundations resting on undrained clay layers, was not observed for the liquefiable layers studied here. A qualitative explanation involves the shear mechanisms of a typical rotational half-cycle, as depicted in figure 14. For experiments where  $B/D_L \geq 1$ , shear mechanisms involved primarily soil outside of the soil column below the structure, as well as a shallow area of soil underneath the edges of the foundation. It is argued that in the areas where shear strains were large, soil behaved in a similar way for all experiments, irrespectively of the weight of the structure. As excess pore water pressures built up, the bearing pressure imposed by the structure was taken up by the soil column directly underneath the foundation (Coelho *et al.*, 2007; Karamitros *et al.*, 2013a). The soil outside of this column liquefied irrespectively of the weight of the structure. Underneath the edges of the foundation, excess pore water pressure was affected by the movement of the structure, exhibiting transient drops (see recordings in figure 11). Drops in pore pressure were on some occasions observed underneath the edge of the foundation that had the tendency to uplift – though actual uplifting was not observed. More importantly, drops in pore pressure were recorded under the downwards moving edge of the foundation due to dilation stemming from excessive shearing of the soil. Though transient drops were recorded, their duration was short and they did not coincide with the time instances of maximum rotation. It was found that one can predict rather well the overall response of excess pore pressure beneath the edge of the foundation by assuming it is similar to that of the free field, at the same depth. Indeed, such a comparison is shown in figure 11. There, the estimated excess pore water pressure, calculated using the excess pore water pressure measured at the same initial depth of the free-field and adjusted to account for the increased settlement of the structure, is superimposed on the excess pore water pressure measured under the edge of the foundation. Though transient drops in pressure could not be captured, the overall pore pressure response was well represented. Thus, the response of the soil that primarily contributed to the rotation-generating shear mechanisms was mostly unaffected by the factor of safety versus vertical load. This could explain why all points in figure 15 follow the same curve, though their calculated factors of safety versus vertical load cover a wide range.

#### Rotational spring approximations

The degradation of normalised secant rocking stiffness as a function of normalised rotation (equations 26 and 27), can be used in simplified methodologies to estimate important characteristics of the rotational response of a shallow foundation that rests on a thin

liquefiable layer during an earthquake. Using the functions proposed here, one can calculate the moment-rotation backbone curve that corresponds to the points of extreme rotation of dynamic moment-rotation loops. Moment-rotation backbone curves can be used for performance-based design, if a value of demanded dynamic moment is known. Importantly, stiffness degradation curves can form the basis of simplified methodologies using rotational springs and dashpots for the calculation of maximum rotation. Such methodologies vary in complexity. For instance, one could use an iterative approximation with an equivalent-linear rotational spring (e.g. Adamidis *et al.*, 2014), an approximation with a non-linear rotational spring (e.g. Anastasopoulos & Kontoroupi, 2014), an approximation following Masing's rules (Masing, 1926), or a more elaborate Bouc-Wen model (Wen, 1976). Here, two examples of such methodologies are given, one using an iterative, equivalent-linear approximation, and one following the extension of Pyke (1979) for Masing's rules.

#### Backbone curves

Moment-rotation backbone curves were calculated for each of the foundations examined experimentally. For the calculation of elastic rocking stiffness (eq. 18), a soil element at a depth of  $B/4$  under the edge of the foundation was considered. It was assumed that the excess pore pressure at this element was the one required to cause full liquefaction at the same depth of the free-field:  $\Delta U = \gamma' B/4$ . This approximation is reasonable for excess pore pressure at that location, as shown in figure 11. Embedment at the beginning of each earthquake was taken into account. Increase of embedment, settlement of the structure, and densification of sand during an earthquake were not considered, although known, as these parameters would not typically be available for the estimation of rotational response. However, if such estimations exist, for instance following Bray & Macedo (2017) or Bullock *et al.* (2019b) for the settlement of the structure, taking them into account is expected to increase the reliability of results.

The backbone-moment rotation curves that correspond to the calculated stiffness degradation curves are shown in figure 16 for all experiments. There, it can be seen that they capture rather well the extreme points of moment-rotation loops for all experiments with  $B/D_L \geq 1$ , irrespectively of the depth of the layer and the weight of the structure. For deep layers with  $B/D_L < 1$ , which were excluded from consideration in this method, the moment-rotation backbone curves are only appropriate when a rocking response is established, as in EQ2 of experiment OA5.

#### Equivalent linear approximation

A simple rotational spring methodology, using an iterative, equivalent-linear approximation was considered. The differential equation that describes the rotational response of a rigid body with a rotational spring and dashpot at its base was used. The time history of acceleration  $A(t)$  at the base of the liquefiable layer was selected as an input, given that it is the easiest to estimate and that we are restricting the method to shallow layers with  $B/D_L \geq 1$ , which will not allow significant change in acceleration within the soil column between the base of the layer and the foundation. If  $I_0$  is the mass moment of inertia around the centre of the foundation:

$$I_0 \ddot{\theta} + C_R \dot{\theta} + K_R \theta - mgh_{CM} \sin \theta = mA(t)h_{CM} \cos \theta \quad (28)$$

The values of  $K_R$  and  $C_R$  were altered for each iteration, based on an 'input' rotation  $\theta$  that was calculated from the previous iteration. Equations 26 and 27 were used to calculate  $K_R$ ,



while the damping ratio for the calculation of  $C_R$  was taken from equation 9. Values of stiffness and damping for the first iteration corresponded to  $\theta=0$ . Figure 17 shows an example application of the method, for the first earthquake of experiment OA6. Figures 17a, b, and c, depict the moment-rotation loops calculated for the 1<sup>st</sup>, 6<sup>th</sup>, and 12<sup>th</sup> iteration respectively.

As with all iterative processes, some consideration on convergence is necessary. In figure 17d, the process of convergence is depicted. The abscissa shows the ‘input’ rotation  $\theta$ , based on which  $K_R$  and  $C_R$  were calculated, and the ordinate shows the ‘output’ rotation  $y(\theta)$ , which is the maximum rotation calculated from the solution of equation 28 for the given values of  $K_R$  and  $C_R$ . Convergence is achieved when  $y(\theta)=\theta$ . Here, due to the pseudo-harmonic nature of the input motion and the linear spring used for each iteration, a value of stiffness existed for which resonance occurred: at ‘input’ rotation  $\theta_{y,max}$  the output rotation  $y(\theta)$  was maximised. The value of  $\theta_{y,max}$  could easily be estimated in advance, as it corresponds to the rocking stiffness for which the natural frequency of the system

$f_n = \frac{1}{2\pi} \sqrt{\frac{K_R}{I_O}}$  coincides with the predominant frequency of the input motion, here equal to 1 Hz in prototype scale. For input rotations  $\theta < \theta_{y,max}$ , fixed-point iterations, where the maximum rotation calculated in an iteration ( $y(\theta_i)$ ) is used as the input rotation for the next iteration ( $\theta_{i+1}$ ), worked well. However, the downwards branch of  $y(\theta)$  for  $\theta > \theta_{y,max}$  could lead to very slow convergence or even ‘lock’ the fixed-point iterations between two values of  $\theta$ . To remedy this issue, a Newton-Raphson inspired process was used. At iteration  $i$ , if  $\theta_i > \theta_{y,max}$ , instead of using  $y(\theta_i)$  as the ‘input’ rotation for iteration  $i+1$ , the tangent of  $y(\theta)$  at  $\theta_i$  was calculated and its intersection with  $y(\theta)=\theta$  was chosen as the ‘input’ rotation  $\theta_{i+1}$  for the new iteration. This process led to quick convergence once  $\theta > \theta_{y,max}$ , as shown graphically in figure 17d. In the case of realistic, non-harmonic earthquake input motions, fixed-point iterations could be sufficient.

Upon convergence, an estimation for maximum rotation was attained. Of equal importance is the estimation of residual tilt at the end of an earthquake. This was done here in a simplistic manner, following Masing’s rule for unloading (Masing, 1926). If the moment-rotation point  $(M_c, \theta_c)$  corresponds to the maximum rotation calculated and the function  $F_{bb}(\theta)$  describes the moment-rotation backbone curve, then the unloading curve is described by the following expression:

$$\frac{M - M_c}{2} = F_{bb}\left(\frac{\theta - \theta_c}{2}\right) \quad (29)$$

Demanding that  $M=0$  in equation 29 yields a typically conservative estimation for residual tilt, as shown in figure 17c.

The performance of the proposed equivalent-linear approximation was assessed not only for the 10 seismic events modelled in the experiments presented so far, but also for 70 additional seismic events extracted from the FLIQ database (Allmond et al., 2015). This database contains results from centrifuge experiments performed at UC Davis. From within the database, results from centrifuge tests coded SHD01, SHD02, JDA01, and JDA02 were examined, as relevant to the problem studied here. The soil profile of all tests selected

consisted of a deep layer of dense Nevada sand, overlain by a shallow, liquefiable layer of looser Nevada sand, and a thin crust of either dense Monterey sand (SHD01, SHD02), dense Nevada sand (JDA01, JDA02), or aquarium gravel (JDA01). The soil was in all cases fully saturated, though the viscosity of the pore fluid used was lower than that required to fully match dynamic and dissipation time scaling. Multiple structures were examined within each centrifuge test, and it was assumed that interaction between structures was insignificant. The structures selected to be examined here were those with shallow, mat foundations. Foundations were typically embedded within the top crust, though two structures of JDA01 they were placed directly on the surface. The structures varied significantly in aspect ratio, ranging from  $h_{CM} / B = 0.34$  to  $h_{CM} / B = 1.90$ , and in bearing pressure, ranging from  $q = 75$  kPa to  $q = 260$  kPa. Scaled acceleration time histories from real earthquakes were typically used as excitations (e.g. Port Island event), and each test was subjected to a sequence of multiple events, typically of increasing intensity. Detailed test descriptions and data reports are provided within the database (Allmond *et al.*, 2015).

The proposed functions for rocking stiffness degradation (equations 26 and 27) and damping ratio degradation (eq. 9) were used within the iterative equivalent-linear approximation to estimate maximum and residual rotation for the structures of the FLIQ database. An effort was made to maintain consistency with the use of the methodology for the centrifuge experiments presented in this paper. The input acceleration used was that recorded at the base of the liquefiable layer. Estimations of embedment and density were made before each event, based on settlement recordings, in the same way as for the experiments presented here. Small strain shear modulus for Nevada sand was defined to match the resonant column results reported by Arulmoli *et al.* (1992) for Nevada sand of 40% relative density, using the function of void ratio  $f(e)$  of equation 11, as proposed Hardin & Drnevich (1972). The expression used was the following:

$$G_{max,Nevada} = 275 p'_{ref} f(e) \left( \frac{p'}{p'_{ref}} \right)^{0.50} \quad (30)$$

Several significant simplifications were made in the use of the proposed methodology to estimate the maximum and residual rotation of the FLIQ experiments. Notably, the rotational response of the structures was estimated as if their foundations were strips, since the proposed methodology was developed for strip foundations. In reality, the foundations of SHD01 and SHD02 were rectangular, with a length of  $1.5B$  and the foundations of JDA01 and JDA02 were square. Resulting differences in rocking stiffness estimation are not prohibitive for this exercise, but are noteworthy. Referring to Gazetas *et al.* (2013) one can easily quantify that in the case of a rectangular foundation of length  $1.5B$ , the rocking stiffness calculated using a formula for a strip is 11% lower than the actual one, while for a square foundation, it is 14% lower than the actual one. Moreover, it was assumed that the surface crust consisted of the same soil as the liquefiable layer, following the observations of Anastasopoulos *et al.* (2012), who showed that for low ratios of dense crust thickness over loose layer depth, the increase in rotational stiffness compared to that of a loose layer of the total depth is small. In addition, the analytical relation used for stiffness assumed a rigid layer at the base of the liquefiable layer. In reality, a layer of dense sand was in place instead of a rigid one. Finally, the structures were simplistically assumed to respond as rigid bodies. When liquefaction occurs, soil softening will drive the fundamental natural period of the soil-structure system far from the fixed-base one, making the structure respond more like a rigid block. Indeed, studying the settlement response of structures with shallow foundations,

Karimi *et al.* (2018) show that the fixed-base fundamental period of the structure is a practically unimportant parameter. However, caution is required for very ‘soft’ structures, where it could become important.

Results of the comparison of maximum and residual rotation, as estimated using the equivalent-linear approximation and as measured in the considered centrifuge tests, are included in figure 18. The equivalent-linear approximation delivered favourable estimations of maximum rotation for the majority of seismic events considered (fig. 18a). Expectedly, it performed better for experiments OA, which were used to develop the stiffness and damping degradation expressions. It offered better estimations for the first earthquake of these tests, for which properties such as soil density and foundation embedment were better known, and importantly, initial tilt was not significant. Estimations for the tests of the FLIQ database were mostly favourable. For instance, the maximum rotation of all events of test JDA02 was captured adequately. Nevertheless, maximum rotation was overestimated for some events, for which significant seismic loading led to unexpectedly low rotation in the experiments. These events corresponded to earthquakes late within the long sequences of motions applied in the FLIQ experiments. It is likely that before these events, significant densification and increase in embedment had taken place. Not appropriately accounting for these changes likely led to lower rocking stiffness and damping ratios than required. As expected from figure 17c, estimations of residual rotation are on the conservative side for almost all events (fig. 18b). Overall, the proposed method performed rather well in the often elusive endeavour of estimating maximum and residual tilt for foundations on liquefiable ground. Estimations were more reliable for foundations which were not significantly tilted prior to seismic loading.

#### Pyke approximation

Though the iterative, equivalent-linear methodology described above performed rather well, one more rotational spring approximation is presented, to showcase that the results of a simplified methodology will depend not only on the proposed stiffness degradation curves but also on the formulation of the methodology itself. A non-linear rotational spring is introduced, following the extension of Masing’s rules (Masing, 1926) that was proposed by Pyke (1979). During initial loading, the spring follows the backbone curve. Upon unloading or reloading, the spring follows a curve that takes the shape of the backbone and is scaled by a factor  $C_p$ , instead of the factor of 2 suggested by Masing (eq. 29). The factor  $C_p$  is defined as follows:

$$C_p = \left| \pm 1 - \frac{M_c}{M_{100}} \right| \quad (31)$$

where  $M_c$  is the moment at the point where loading is reversed and  $M_{100}$  is the moment on the backbone curve for  $\frac{\theta}{\theta_{s,el}} = 100$ , taken here as a reference ‘strength’. The unit term is negative for unloading and positive for reloading.

By defining  $K_R$  to follow the above requirements and setting  $C_R = 0$ , equation 28 was solved. The solution corresponding to the first earthquake of test OA6 is presented in figure 19. In this example, the approximation performs favourably for maximum and residual tilt. Obviously, this approximation does not allow for control of damping ratio. The area contained within the loops is the outcome of the shape imposed on unloading and reloading branches.

Concentrated results for estimations of maximum and residual rotation for the experiments presented here as well as for those of the FLIQ database (Allmond *et al.*, 2015) are given in figure 20. While this method performed favourably for the first earthquake of experiments OA, its estimations for the second earthquake were less reliable. When starting at an increased initial inclination, this method tended to overpredict the accumulation of rotation in one direction, delivering over-conservative estimates. The same was true for the results of the FLIQ database. There, rotation estimations for events later in the sequence of applied motions were in some cases larger than the maximum of 0.14 rad presented in the figure. Overall, this method should only be used for foundations where no initial tilt exists. It is less reliable than the equivalent-linear one for very long or multiple events, and for significantly asymmetrical input motions.

### Conclusions

In the event of earthquake-induced liquefaction, structures with shallow foundations can settle and tilt excessively. Though a wealth of publications has looked on settlement, less attention has so far been given to the rotational response. Here, results from seven dynamic centrifuge tests are presented, focusing on this problem. A rocking rotational response was established in all experiments with thin liquefiable layers, whose depth was equal to or less than the width of the structure examined. For deeper layers, the establishment of a rocking response depended on the bearing pressure applied by the foundation and its embedment, with heavier and more deeply embedded structures responding by rocking.

Focusing on rocking response, values of secant rocking stiffness and damping ratio were calculated from the experimental results. While rocking stiffness was expectedly dependent on the bearing pressure of the structure, the depth of the liquefiable layer was not as important. Consistently to what has been observed for non-liquefiable soil layers, secant rocking stiffness reduced with increasing rotation.

A normalisation methodology for rocking stiffness and rotation was proposed, based on estimations of elastic rotational stiffness. To apply the proposed normalisation, sensible estimations were made for the shear modulus and the factor of safety versus vertical load for each half-cycle examined. All points of normalised rocking stiffness versus normalised rotation coincided on a single attenuation curve, irrespective of the factor of safety versus vertical load. Expressions that fit the experimental results were proposed and used to derive moment-rotation backbone curves that compared favourably with experimental results.

The proposed expressions for rocking stiffness attenuation can be used in the development of simplified methodologies for the evaluation of important characteristics of rocking response in the event of liquefaction. Here, two examples of such simplified methodologies were presented, one using an iterative, equivalent-linear approximation, and one using an approximation based on the extension of Masing's rules (Masing, 1926) proposed by Pyke (1979). The methodologies were assessed for their performance versus the centrifuge test results presented here and also versus the rotation time-histories recorded in 70 seismic events extracted from four centrifuge tests included in the FLIQ database (Allmond *et al.*, 2015). The equivalent-linear approximation performed adequately in the estimation of maximum rotation for the majority of events. In some events from the FLIQ database, maximum rotation was overpredicted, due to not appropriately accounting for the increase in initial stiffness caused by densification and increase of embedment after a series of multiple seismic events. Residual tilt at the end of the earthquake was simplistically estimated based on the maximum rotation, assuming unloading according to Masing (Masing, 1926). Estimations of residual tilt at the end of the earthquake were conservative but not overly so. The approximation following Pyke (1979) performed well only for earthquakes in the beginning

of a sequence of multiple motions. If initial tilt was present for a motion, this methodology could significantly overpredict accumulated tilt. Though initial tilt is not typically present when studying the rocking response of a structure on a liquefiable layer, the equivalent-linear method was overall more reliable and is expected to perform well in predictions of maximum and residual tilt of a shallow strip foundation resting on a thin liquefiable layer.

Certain important limitations must be taken into account when applying the methodologies proposed here. Initially, the proposed expressions for rocking stiffness degradation cannot be reliably used for layers where  $B/D_L < 1$ . In these cases, foundations are not certain to respond with rocking, possibly leading to severe overestimation of rotation if the presented methods are used. Secondly, the rocking stiffness attenuation expressions derived here refer to strip foundations. Though the examined methodologies were shown to perform adequately for the rectangular and square foundations of the FLIQ database, caution is required in the extension of the given expressions for non-strip foundations. Thirdly, the method was only developed for and assessed with layers of clean sand. In cases of layers with lower permeability, e.g. for silty sands, the stiffness attenuation could change. Moreover, significant post-liquefaction tilting could occur (Ishikawa *et al.*, 2015), which will not be captured. Attention is also required when the rotational spring methodologies examined here are used for foundations that have a significant initial inclination, as in such cases they can perform poorly. Finally, structures were modelled as rigid bodies. Though this assumption is expected to be sufficient in most cases where soil liquefaction causes substantial soil softening, the fundamental fixed-base period of a particularly 'soft' structure might have to be taken into account.

#### Acknowledgements

The centrifuge tests were carried out with the excellent assistance of the technicians of the Schofield Centre, who are hereby acknowledged.

#### Nomenclature

$B$	Width of foundation
$D_L$	Liquefaction depth
$h_{CM}$	Height of centre of mass from base of foundation
$q$	Bearing pressure applied by the structure
$S$	Settlement
$e$	Void ratio
$G_s$	Specific gravity of solids
$k$	Permeability
$M$	Moment
$g$	Acceleration of gravity
$I_{CM}$	Mass moment of inertia around centre of mass
$I_O$	Mass moment of inertia around centre of foundation
$m$	Mass

$V$	Weight of structure
$G$	Shear modulus
$p'$	Mean effective stress
$K_R$	Secant rocking stiffness coefficient
$C_R$	Rocking damping coefficient
$C_P$	Pyke factor for unloading/reloading
$F_S$	Factor of safety versus vertical load
$q_f$	Ultimate load
$q'_{over}$	Overburden effective stress
$A(t)$	Time history of input acceleration
$d_{(x)}$	Particle size for which (x) % of the material is finer
$a_{CM_x}$	Horizontal component of acceleration at the centre of mass, in local coordinates
LVDT	Linear Variable Displacement Transducer
PIV	Particle Image Velocimetry
PPT	Pore Pressure Transducer
MEMS	MicroElectroMechanical systems accelerometer
Acc	Piezoelectric accelerometer
$\gamma$	Shear strain
$\Delta U$	Excess pore water pressure
$\phi_{crit}$	Critical state friction angle
$\theta$	Rotation angle
$\theta_s$	Reference rotation
$\gamma'_s$	Buoyant saturated unit weight
$\nu$	Poisson's ratio

## References

- Adamidis, O. (2017). Earthquake-induced liquefaction of sand and response of structures with shallow foundations. Ph.D. thesis, University of Cambridge, Cambridge, UK.
- Adamidis, O., Alber, S. & Anastasopoulos, I. (2020). Assessment of three-dimensional printing of granular media for geotechnical applications. *Geotechnical Testing Journal* **43**, No. 3, DOI: 10.1520/GTJ20180259.
- Adamidis, O., Gazetas, G., Anastasopoulos, I. & Argyrou, C. (2014). Equivalent-linear stiffness and damping in rocking of circular and strip foundations. *Bulletin of Earthquake Engineering* **12**, No. 3, 1177–1200, DOI: 10.1007/s10518-013-9554-0, <http://link.springer.com/10.1007/s10518-013-9554-0>.
- Adamidis, O. & Madabhushi, G. S. P. (2015). Use of viscous pore fluids in dynamic centrifuge modelling. *International Journal of Physical Modelling in Geotechnics* **15**, No. 3, 141–149, DOI: 10.1680/ijpmg.14.00022, <http://www.icevirtuallibrary.com/content/article/10.1680/ijpmg.14.00022>.
- Adamidis, O. & Madabhushi, S. P. G. (2018a). Deformation mechanisms under shallow foundations on liquefiable layers of varying thickness. *Géotechnique* **68**, No. 7, 602–613, DOI: 10.1680/jgeot.17.P.067, <http://www.icevirtuallibrary.com/doi/10.1680/jgeot.17.P.067>.
- Adamidis, O. & Madabhushi, S. P. G. (2018b). Experimental investigation of drainage during earthquake-induced liquefaction. *Géotechnique* **68**, No. 8, 655–665, DOI: 10.1680/jgeot.16.P.090, <http://www.icevirtuallibrary.com/doi/10.1680/jgeot.16.p.090> <https://www.icevirtuallibrary.com/doi/10.1680/jgeot.16.P.090>.
- Allmond, J., Kutter, B. L., Bray, J. & Hayden, C. (2015). New Database for Foundation and Ground Performance in Liquefaction Experiments. *Earthquake Spectra* **31**, No. 4, 2485–2509, DOI: 10.1193/072814EQS120, <http://earthquakespectra.org/doi/10.1193/072814EQS120>.
- Anastasopoulos, I., Gazetas, G., Loli, M., Apostolou, M. & Gerolymos, N. (2010). Soil failure can be used for seismic protection of structures. *Bulletin of Earthquake Engineering* **8**, No. 2, 309–326, DOI: 10.1007/s10518-009-9145-2.
- Anastasopoulos, I. & Kontoroupi, T. (2014). Simplified approximate method for analysis of rocking systems accounting for soil inelasticity and foundation uplifting. *Soil*

- Dynamics and Earthquake Engineering **56**, 28–43, DOI:  
10.1016/j.soildyn.2013.10.001, <http://dx.doi.org/10.1016/j.soildyn.2013.10.001>.
- Anastasopoulos, I., Kourkoulis, R., Gelagoti, F. & Papadopoulos, E. (2012). Rocking response of SDOF systems on shallow improved sand: An experimental study. Soil Dynamics and Earthquake Engineering **40**, 15–33, DOI:  
10.1016/j.soildyn.2012.04.006, <http://dx.doi.org/10.1016/j.soildyn.2012.04.006>.
- Andrawes, K. Z., Al-Omari, R. R. & Kirkpatrick, W. M. (1996). Bearing capacity of a strip foundation on a sand layer overlying a smooth rigid stratum. Geotechnical and Geological Engineering **14**, 227–236.
- Arulmoli, K., Muraleetharan, K. K., Hosain, M. M. & Fruth L. S. (1992). VELACS: Laboratory Testing Program Soil Data Report. Technical report, The Earth Technology Corporation, Irvine, California.
- Ayoubi, P. & Pak, A. (2017). Liquefaction-induced settlement of shallow foundations on two-layered subsoil strata. Soil Dynamics and Earthquake Engineering **94**, No. January, 35–46, DOI: 10.1016/j.soildyn.2017.01.004,  
<http://dx.doi.org/10.1016/j.soildyn.2017.01.004>.
- Azeiteiro, R. J. N., Coelho, P. A. L. F., Taborda, D. M. G. & Grazina, J. C. D. (2017). Critical State-Based Interpretation of the Monotonic Behavior of Hostun Sand. Journal of Geotechnical and Geoenvironmental Engineering **143**, No. 5, 04017004, DOI: 10.1061/(ASCE)GT.1943-5606.0001659,  
<http://ascelibrary.org/doi/10.1061/%28ASCE%29GT.1943-5606.0001659>.
- Bertalot, D. & Brennan, A. (2015). Influence of initial stress distribution on liquefaction-induced settlement of shallow foundations. Géotechnique **65**, No. 5, 418–428, DOI: 10.1680/geot.SIP.15.P.002,  
<http://www.icevirtuallibrary.com/doi/full/10.1680/geot.SIP.15.P.002%5Cnhttp://www.icevirtuallibrary.com/doi/pdf/10.1680/geot.SIP.15.P.002>.
- Bertalot, D., Brennan, A. & Villalobos, F. (2013). Influence of bearing pressure on liquefaction-induced settlement of shallow foundations. Géotechnique **63**, No. 5, 391–399, DOI: 10.1680/geot.11.P.040,  
<http://www.icevirtuallibrary.com/doi/10.1680/geot.11.P.040>.



- Bray, J. D. & Macedo, J. (2017). 6th Ishihara lecture: Simplified procedure for estimating liquefaction-induced building settlement. *Soil Dynamics and Earthquake Engineering* **102**, No. August, 215–231, DOI: 10.1016/j.soildyn.2017.08.026.
- Bray, J. D., Sancio, R. B., Durgunoglu, T., Onalp, A., Youd, T. L., Stewart, J. P., Seed, R. B., Cetin, O. K., Bol, E., Baturay, M. B., Christensen, C. & Karadayilar, T. (2004). Subsurface Characterization at Ground Failure Sites in Adapazari, Turkey. *Journal of Geotechnical and Geoenvironmental Engineering* **130**, No. 7, 673–685, DOI: 10.1061/(ASCE)1090-0241(2004)130:7(673).
- Brennan, A. J., Thusyanthan, N. I. & Madabhushi, S. P. (2005). Evaluation of Shear Modulus and Damping in Dynamic Centrifuge Tests. *Journal of Geotechnical and Geoenvironmental Engineering* **131**, No. 12, 1488–1497, DOI: 10.1061/(ASCE)1090-0241(2005)131:12(1488).
- Bullock, Z., Dashti, S., Karimi, Z., Liel, A., Porter, K. & Franke, K. (2019a). Probabilistic models for residual and peak transient tilt of mat-founded structures on liquefiable soils. *Journal of Geotechnical and Geoenvironmental Engineering* **145**, No. 2, DOI: 10.1061/(ASCE)GT.1943-5606.0002002.
- Bullock, Z., Karimi, Z., Dashti, S., Porter, K., Liel, A. B. & Franke, K. W. (2019b). A physics-informed semi-empirical probabilistic model for the settlement of shallow-founded structures on liquefiable ground. *Géotechnique* **f69**, No. 5, 406–419, DOI: 10.1680/jgeot.17.P.174, <https://www.icevirtuallibrary.com/doi/10.1680/jgeot.17.P.174>.
- Butterfield, R. & Gottardi, G. (1994). A complete three-dimensional failure envelope for shallow footings on sand. *Géotechnique* **44**, No. 1, 181–184, DOI: 10.1680/geot.1994.44.1.181.
- Chatzigogos, C. T., Pecker, A. & Salençon, J. (2009). Macroelement modeling of shallow foundations. *Soil Dynamics and Earthquake Engineering* **29**, No. 5, 765–781, DOI: 10.1016/j.soildyn.2008.08.009, 0802.0425.
- Coelho, P. A. L. F., Haigh, S. K., Gopal Madabhushi, S. P. & O'brien, T. S. (2007). Post-earthquake behaviour of footings employing densification to mitigate liquefaction. *Proceedings of the ICE - Ground Improvement* **11**, No. 1, 45–53, DOI: 10.1680/grim.2007.11.1.45.

- Cubrinovski, M., Bradley, B., Wotherspoon, L., Green, R., Bray, J., Wood, C., Pender, M., Allen, J., Bradshaw, A., Rix, G., Taylor, M., Robinson, K., Henderson, D., Giorgini, S., Ma, K., Winkley, A., Zupan, J., O'Rourke, T., DePascale, G. & Wells, D. (2011). Geotechnical aspects of the 22 February 2011 Christchurch earthquake. *Bulletin of the New Zealand Society for Earthquake Engineering* **44**, No. 4, 205–226.
- da Silva Marques, A. S. P., de Figueiredo Coelho, P. A. L., Haigh, S. & Madabhushi, G. (2014). Centrifuge Modeling of Liquefaction Effects on Shallow Foundations. In *Seismic Evaluation and Rehabilitation of Structures* (Ilki, A. & Fardis, M., eds.), Cham, Switzerland: Springer, pp. 425–440, DOI: 10.1007/978-3-319-00458-7\_24, [http://link.springer.com/10.1007/978-3-319-00458-7\\_24](http://link.springer.com/10.1007/978-3-319-00458-7_24).
- Dabeet, A., Wijewickreme, D. & Byrne, P. (2012). Simulation of cyclic direct simple shear loading response of soils using discrete element modeling. In *15th World Conference on Earthquake Engineering*, Lisbon, Portugal: Curran Associates, New York.
- Dashti, S., Bray, J., Pestana, J., Riemer, M. & Wilson, D. (2010a). Centrifuge Testing to Evaluate and Mitigate Liquefaction-Induced Building Settlement Mechanisms. *Journal of Geotechnical and Geoenvironmental Engineering* **136**, No. 7, 918–929, DOI: 10.1061/(ASCE)GT.1943-5606.0000306, [http://dx.doi.org/10.1061/\(ASCE\)GT.1943-5606.0000306](http://dx.doi.org/10.1061/(ASCE)GT.1943-5606.0000306), [http://ascelibrary.org/doi/abs/10.1061/\(ASCE\)GT.1943-5606.0000306](http://ascelibrary.org/doi/abs/10.1061/(ASCE)GT.1943-5606.0000306), [http://ascelibrary.org/doi/pdf/10.1061/\(ASCE\)GT.1943-5606.0000306](http://ascelibrary.org/doi/pdf/10.1061/(ASCE)GT.1943-5606.0000306).
- Dashti, S., Bray, J. D., Pestana, J. M., Riemer, M. & Wilson, D. (2010b). Mechanisms of Seismically Induced Settlement of Buildings with Shallow Foundations on Liquefiable Soil. *Journal of Geotechnical and Geoenvironmental Engineering* **136**, No. 1, 151–164, DOI: 10.1061/(ASCE)GT.1943-5606.0000179.
- Elgamal, A., Zeghal, M., Taboada, V. & Dobry, R. (1996). Analysis of Site Liquefaction and Lateral Spreading Using Centrifuge Testing Records. *Soils and Foundations* **36**, No. 2, 111–121, DOI: 10.3208/sandf.36.2\_111, [http://joi.jlc.jst.go.jp/JST.Journalarchive/sandf1995/36.2\\_111?from=CrossRef](http://joi.jlc.jst.go.jp/JST.Journalarchive/sandf1995/36.2_111?from=CrossRef).
- Gajan, S. & Kutter, B. L. (2009). Effects of Moment-to-Shear Ratio on Combined Cyclic Load-Displacement Behavior of Shallow Foundations from Centrifuge Experiments. *Journal of Geotechnical and Geoenvironmental Engineering* **135**, No. 8, 1044–1055,

DOI: 10.1061/(ASCE)GT.1943-5606.0000034,

<http://ascelibrary.org/doi/10.1061/%28ASCE%29GT.1943-5606.0000034>.

Gajan, S., Kutter, B. L., Phalen, J. D., Hutchinson, T. C. & Martin, G. R. (2005). Centrifuge modeling of load-deformation behavior of rocking shallow foundations. *Soil Dynamics and Earthquake Engineering* **25**, No. 7-10, 773–783, DOI: 10.1016/j.soildyn.2004.11.019.

Gazetas, G. (1983). Analysis of machine foundation vibrations: State of the art. *International Journal of Soil Dynamics and Earthquake Engineering* **2**, No. 1, 2–42, DOI: 10.1016/0261-7277(83)90025-6.

Gazetas, G. (1991). Formulas and Charts for Impedances of Surface and Embedded Foundations. *Journal of Geotechnical Engineering* **117**, No. 9, 1363–1381, DOI: 10.1061/(ASCE)0733-9410(1991)117:9(1363).

Gazetas, G., Anastasopoulos, I., Adamidis, O. & Kontoroupi, T. (2013). Nonlinear rocking stiffness of foundations. *Soil Dynamics and Earthquake Engineering* **47**, No. April, 83—91, DOI: 10.1016/j.soildyn.2012.12.011.

Hardin, B. O. & Drnevich, V. P. (1972). Shear Modulus and Damping in Soils: Design Equations and Curves. *Journal of the Soil Mechanics and Foundations Division* **98**, No. 7, 667–692, [https://www.cambridge.org/core/product/identifier/S000748530002229X/type/journal\\_article](https://www.cambridge.org/core/product/identifier/S000748530002229X/type/journal_article).

Heron, C., Haigh, S. & Madabhushi, S. (2015). A new macro-element model encapsulating the dynamic moment–rotation behaviour of raft foundations. *Géotechnique* **65**, No. 5, 442–451, DOI: 10.1680/geot.SIP.15.P.020, <http://www.icevirtuallibrary.com/doi/full/10.1680/geot.SIP.15.P.020%5Cnhttp://www.icevirtuallibrary.com/doi/pdf/10.1680/geot.SIP.15.P.020>.

Housner, G. W. (1963). The behavior of inverted pendulum structures during earthquakes. *Bulletin of the Seismological Society of America* **53**, No. 2, 403–417, DOI: 10.1017/CBO9781107415324.004, arXiv:1011.1669v3.

Ishibashi, I. & Zhang, X. (1993). Unified dynamic shear moduli and damping ratios of sand and clay. *Soils and Foundations* **33**, No. 1, 182–191, DOI: 10.3208/sandf1972.33.182, <http://joi.jlc.jst.go.jp/JST.Journalarchive/sandf1972/33.182?from=CrossRef>.

Ishikawa, A., Zhou, Y.-G., Shamoto, Y., Mano, H., Chen, Y.-M. & Ling, D.-S. (2015).

Observation of post-liquefaction progressive failure of shallow foundation in centrifuge model tests. *Soils and Foundations* **55**, No. 6, 1501–1511, DOI: 10.1016/j.sandf.2015.10.014, <http://dx.doi.org/10.1016/j.sandf.2015.10.014> <https://linkinghub.elsevier.com/retrieve/pii/S0038080615001729>.

Jakub, M. & Roeset, J. M. (1977a). Dynamic Stiffness of Foundations: 2-D vs 3-D Solutions. Technical report, MIT.

Jakub, M. & Roeset, J. M. (1977b). Nonlinear Stiffness of Foundations. Technical report, MIT.

Karamitros, D. K., Bouckovalas, G. D. & Chaloulos, Y. K. (2013a). Insight into the Seismic Liquefaction Performance of Shallow Foundations. *Journal of Geotechnical and Geoenvironmental Engineering* **139**, No. 4, 599–607, DOI: 10.1061/(ASCE)GT.1943-5606.0000797, <http://ascelibrary.org/doi/10.1061/%28ASCE%29GT.1943-5606.0000797>.

Karamitros, D. K., Bouckovalas, G. D. & Chaloulos, Y. K. (2013b). Seismic settlements of shallow foundations on liquefiable soil with a clay crust. *Soil Dynamics and Earthquake Engineering* **46**, 64–76, DOI: 10.1016/j.soildyn.2012.11.012, <http://dx.doi.org/10.1016/j.soildyn.2012.11.012>.

Karamitros, D. K., Bouckovalas, G. D., Chaloulos, Y. K. & Andrianopoulos, K. I. (2013c). Numerical analysis of liquefaction-induced bearing capacity degradation of shallow foundations on a two-layered soil profile. *Soil Dynamics and Earthquake Engineering* **44**, 90–101, DOI: 10.1016/j.soildyn.2012.07.028, <http://dx.doi.org/10.1016/j.soildyn.2012.07.028>.

Karimi, Z. & Dashti, S. (2016). Seismic performance of shallow founded structures on liquefiable ground: Validation of numerical simulations using centrifuge experiments. *Journal of Geotechnical and Geoenvironmental Engineering* **142**, No. 6, 4016011, DOI: 10.1061/(ASCE)GT.1943-5606.0001479, <http://ascelibrary.org/doi/abs/10.1061/%28ASCE%29GT.1943-5606.0001479>.

Karimi, Z., Dashti, S., Bullock, Z., Porter, K. & Liel, A. (2018). Key predictors of structure settlement on liquefiable ground: a numerical parametric study. *Soil Dynamics and Earthquake Engineering* **113**, No. April 2017, 286–308, DOI:

- 10.1016/j.soildyn.2018.03.001,  
<https://linkinghub.elsevier.com/retrieve/pii/S0267726117303974>.
- Kokkali, P., Anastasopoulos, I., Abdoun, T. & Gazetas, G. (2014). Static and cyclic rocking on sand: centrifuge versus reduced-scale 1 g experiments. *Géotechnique* **64**, No. 11, 865–880, DOI: 10.1680/geot.14.P.064,  
<http://www.icevirtuallibrary.com.libproxy1.nus.edu.sg/content/article/10.1680/geot.14.P.064>.
- Kourkoulis, R., Anastasopoulos, I., Gelagoti, F. & Kokkali, P. (2012). Dimensional analysis of SDOF systems rocking on inelastic soil. *Journal of Earthquake Engineering* **16**, No. 7, 995–1022, DOI: 10.1080/13632469.2012.691615.
- Liu, L. & Dobry, R. (1997). Seismic Response of Shallow Foundation on Liquefiable Sand. *Journal of Geotechnical and Geoenvironmental Engineering* **123**, No. 6, 557–567, DOI: 10.1061/(ASCE)1090-0241(1997)123:6(557), arXiv:1011.1669v3.
- Madabhushi, G. (2014). *Centrifuge Modelling for Civil Engineers*. Boca Raton, FL, USA: CRC Press, Taylor & Francis Group.
- Madabhushi, S., Schofield, A. & Lesley, S. (1998). A new Stored Angular Momentum (SAM) based earthquake actuator. In *Centrifuge 98* (Kimura, T., Kusakabe, O. & Takemura, J., eds.), Tokyo, Japan: Balkema, Rotterdam, pp. 111–116.
- Madabhushi, S. P. G., Houghton, N. E. & Haigh, S. K. (2006). A new automatic sand pourer for model preparation at University of Cambridge. In *Proceedings of the Sixth International Conference on Physical Modelling in Geotechnics*, Taylor and Francis Group, London, pp. 217–222, DOI: 10.1201/NOE0415415866.ch25.
- Mandel, J. & Salençon, J. (1972). Force portante d'un sol sur une assise rigide (étude théorique. *Géotechnique* **22**, No. 1, 79–93, DOI: 10.1680/geot.1972.22.1.79,  
<http://www.icevirtuallibrary.com/doi/10.1680/geot.1972.22.1.79>.
- Masing, G. (1926). Eignespannungen und Verfestigung beim Messing. In *Second International Congress on Applied Mechanics*, Zurich, Switzerland, pp. 332–335.
- Mitrani, H. (2006). *Liquefaction Remediation Techniques for Existing Buildings*. Ph.D. thesis, University of Cambridge.
- Pelekis, I., Madabhushi, G. S. & DeJong, M. J. (2018). Seismic performance of buildings with structural and foundation rocking in centrifuge testing. *Earthquake Engineering and Structural Dynamics* **47**, No. 12, 2390–2409, DOI: 10.1002/eqe.3089.

- Pyke, R. (1979). Non linear soil models for irregular cyclic loadings. *Journal of the geotechnical engineering division* **105**, No. 6, 715–726.
- Steedman, R. S. & Madabhushi, S. P. G. (1991). Wave propagation in sand medium. In *Proceeding of the fourth International Conference on Seismic Zonation*, Palo Alto, CA, USA.
- Stringer, M. E. & Madabhushi, S. P. G. (2009). Novel Computer-Controlled Saturation of Dynamic Centrifuge Models Using High Viscosity Fluids. *Geotechnical Testing Journal* **32**, No. 6, 102435, DOI: 10.1520/GTJ102435, <http://www.astm.org/doiLink.cgi?GTJ102435>.
- Tokimatsu, K., Hino, K., Suzuki, H., Ohno, K., Tamura, S. & Suzuki, Y. (2019). Liquefaction-induced settlement and tilting of buildings with shallow foundations based on field and laboratory observation. *Soil Dynamics and Earthquake Engineering* **124**, No. January 2018, 268–279, DOI: 10.1016/j.soildyn.2018.04.054, <https://doi.org/10.1016/j.soildyn.2018.04.054>.
- Wen, Y. X. (1976). Method for random vibration of hysteretic systems. *Journal of the Engineering Mechanics Division* **102**, No. 2, 249–263.
- White, D., Take, W. & Bolton, M. (2003). Soil deformation measurement using particle image velocimetry ( PIV ) and photogrammetry. *Geotechnique* **53**, No. 7, 619–631, DOI: 10.1680/geot.2003.53.7.619, 1751-7656.
- Yasuda, S., Harada, K., Ishikawa, K. & Kanemaru, Y. (2012). Characteristics of liquefaction in Tokyo Bay area by the 2011 Great East Japan Earthquake. *Soils and Foundations* **52**, No. 5, 793–810, DOI: 10.1016/j.sandf.2012.11.004, <http://dx.doi.org/10.1016/j.sandf.2012.11.004>.
- Youd, T. & Craven, T. (1975). Lateral Stress in Sands During Cyclic Loading. *Journal of the Geotechnical Engineering Division* **101**, No. 2, 217–221.

Table 1. Centrifuge test details

Test ID	Normalised width $B / D_L$	Bearing pressure $q$ (kPa)	Structure type
OA4	0.4	50	a
OA5	0.4	100	b
OA6	1	50	a
OA7	1	100	b
OA8	2	50	a
OA10	2	100	b
OA12	3.9	100	b

Table 2. Properties of Hostun sand. Reproduced from Mitrani (2006) and Adamidis *et al.* (2020).. Permeability was measured at a void ratio of  $e = 0.836$ .

$e_{max}$	$e_{min}$	$d_{50}$	$\frac{d_{60}}{d_{10}}$	$G_s$	$\phi_{crit}$	$k$
1.010	0.555	341 $\mu m$	1.49	2.65	33°	0.92 $\frac{mm}{s}$

Table 3. Properties of structures, in prototype scale.

Structure	Bearing pressure (kPa)	Aspect ratio ( $h_{CM} / B$ )	Fixed-base frequency (Hz)
a	50	0.58	7.4
b	100	0.58	5.9

Table 4. Initial factors of safety versus vertical load.

Test	$B / D_L$	$q(kPa)$	$N_q$	$N_\gamma$	$q_f(kPa)$	$F_s$
OA4	0.4	50	26.1	25	554	11
OA5	0.4	100	26.1	25	624	6
OA6	1	50	32.1	25	736	15
OA7	1	100	32.1	25	706	7
OA8	2	50	91.7	37.5	1198	24
OA10	2	100	91.7	37.5	1306	13
OA12	3.9	100	1122.3	235.8	16434	164

## Figure captions

Figure 1. Cross-section sketches of centrifuge experiments. Dimensions in prototype scale.

Figure 2. Cross-section sketches of the structures in prototype scale.

Figure 3. Fast Fourier Transforms (FFT) for input motion acceleration and acceleration at the top of the structure. The fixed-base frequency (f.b.f.) of each structure is included in the FFT plots. Units in prototype scale.

Figure 4. Moment and settlement refer to the centre of the base of the foundation. Counter-clockwise rotation is considered positive.

Figure 5. Settlement-rotation response for all experiments. Units in prototype scale.

Figure 6. Moment-rotation response for all experiments. The points highlighted correspond to the calculated values of secant rocking stiffness. Units in prototype scale.

Figure 7. Sketch outlining how damping ratio and rocking stiffness were calculated for each half-cycle.

Figure 8. Damping ratio versus (a) amplitude of dynamic rotation and (b) rotation including accumulated tilt.

Figure 9. Cross-section sketch of centrifuge experiments OA2 and OA3. Recordings from the instrumented free-field soil column to the left are used here. Dimensions in prototype scale.

Figure 10. Comparison of  $\mathbf{K}(\gamma)$ , as proposed by Ishibashi & Zhang (1993), with calculated values, using the relation proposed by Azeiteiro *et al.* (2017) for  $G_{max}$ .

Figure 11. Time histories of excess pore water pressure under the right edge of the foundation: measured excess pore pressure versus estimated, using free-field pore pressure and settlement data. Due to a malfunction of the free-field transducer in OA12, an estimation of maximum excess pore pressure was made assuming  $r_u = 1$  at the free-field. Units in prototype scale.

Figure 12. Time histories of shear strain under the foundation. Units in prototype scale.

Figure 13. Rocking stiffness results from all experiments with  $\mathbf{B} / D_L \geq 1$ . Units in prototype scale.

Figure 14. Shear strains accumulated during the 5<sup>th</sup> rotational half-cycle.

Figure 15. Effect of the factor of safety versus vertical load on normalised rotational stiffness degradation and proposed fit.

Figure 16. Moment-rotation response for all experiments with the estimated backbone curves superimposed.

Figure 17. Example application of the iterative, equivalent-linear process for the estimation of maximum rotation. Moment-rotation loops calculated in the (a) 1<sup>st</sup> iteration, (b) 6<sup>th</sup> iteration, and (c) 12<sup>th</sup> iteration are included. The process of convergence is shown in (d). Due to the pseudo-harmonic nature of the input acceleration, resonance occurs for a certain stiffness, leading to maximum rotation  $\theta_{y,max}$ . Fixed-point iterations were performed for rotations lower than  $\theta_{y,max}$ , while for larger rotations a Newton-Raphson inspired method was used, which led to fast convergence. Convergence was achieved within ten iterations (e). Once the maximum rotation was estimated, a prediction for the residual tilt was attempted, shown in (c), following Masing's rules for unloading (Masing, 1926).

Figure 18. Estimated versus experimentally measured (a) maximum rotation and (b) residual rotation, using the iterative, equivalent-linear approximation. The outlined method, which was based on the experimental results presented in this paper (points OA),



performs adequately for the majority of events recorded in the experimental results of centrifuge tests SHD01, SHD02, JDA01, and JDA02, conducted at UC Davis, and included in the FLIQ database (Allmond *et al.*, 2015).

Figure 19. Example application of the Pyke (1979) approximation for moment-rotation loops. Maximum and residual tilt are highlighted.

Figure 20. Estimated versus experimentally measured (a) maximum rotation and (b) residual rotation, using the Pyke (1979) approximation. The comparison includes results from the FLIQ database (Allmond *et al.*, 2015). Rotation was overestimated for events where an initial tilt was present.

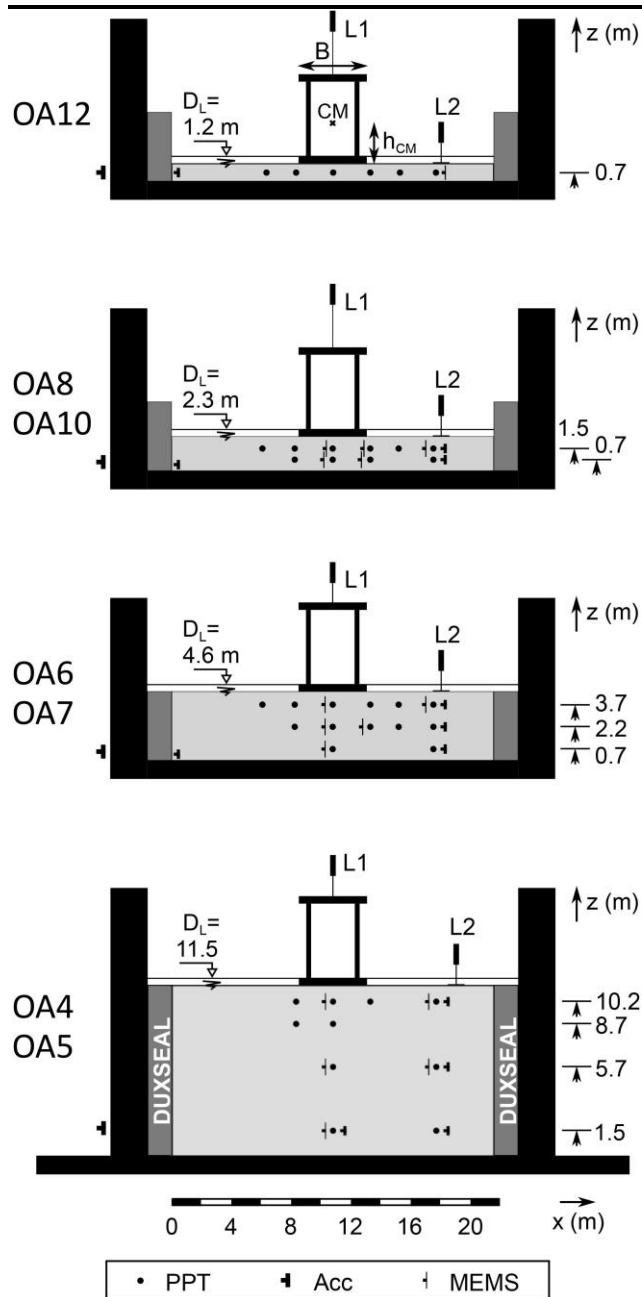


Fig. 1.

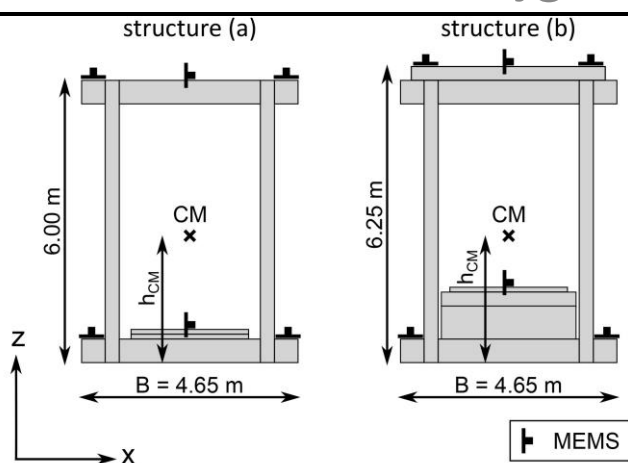


Fig. 2.

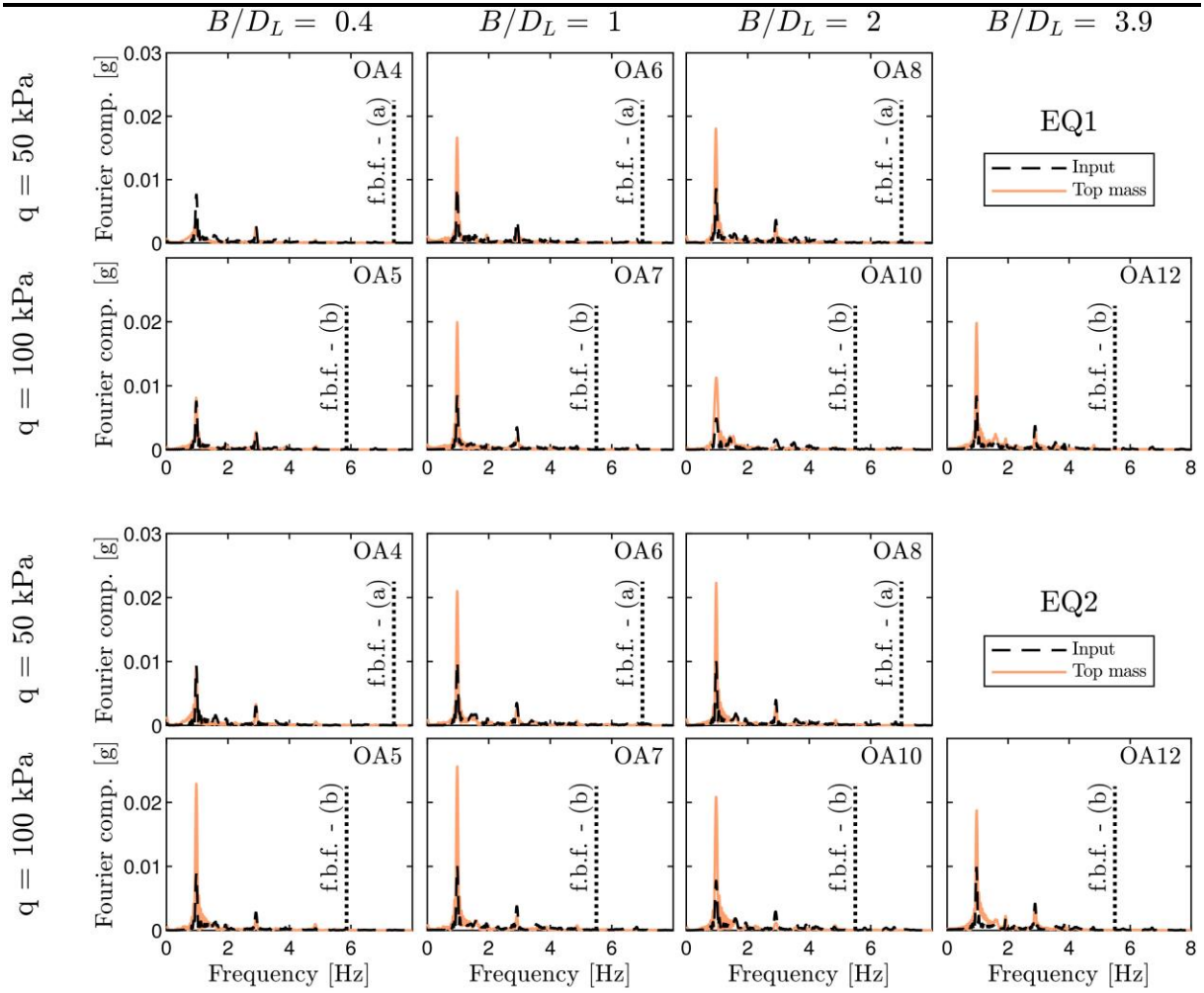


Fig. 3.

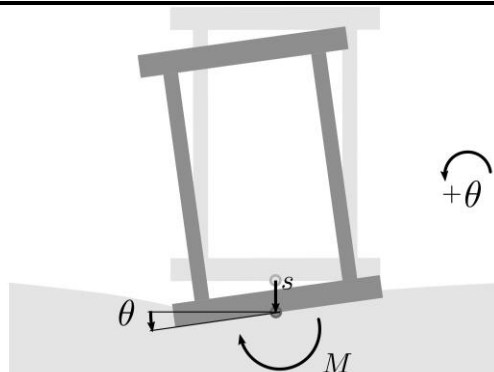


Fig. 4.

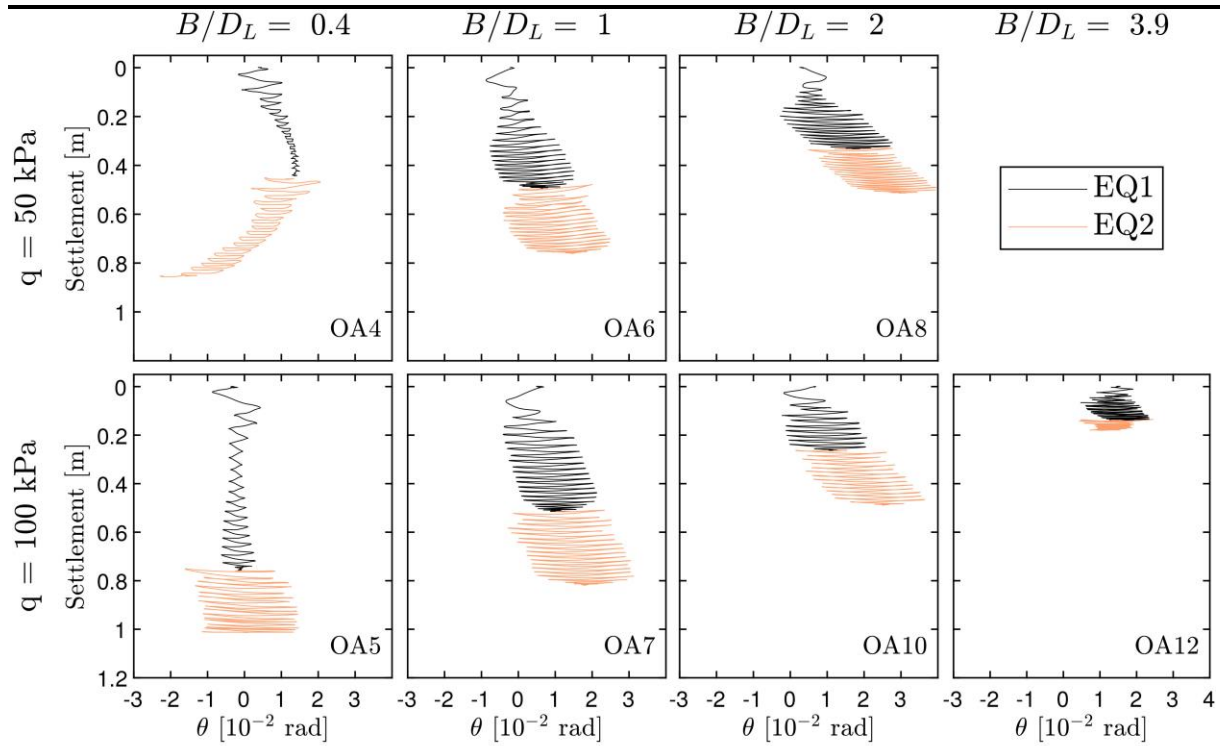


Fig. 5.

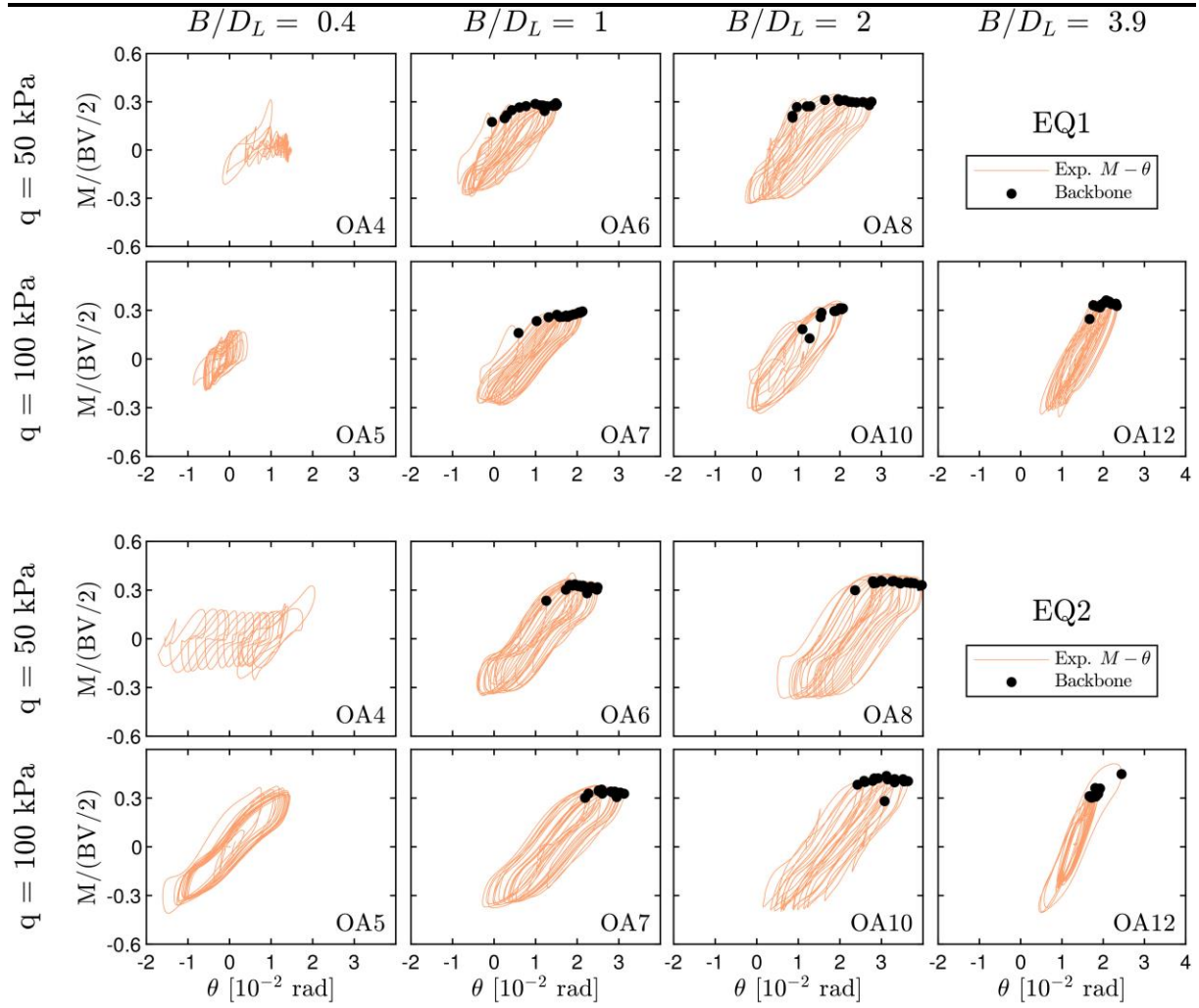


Fig. 6.

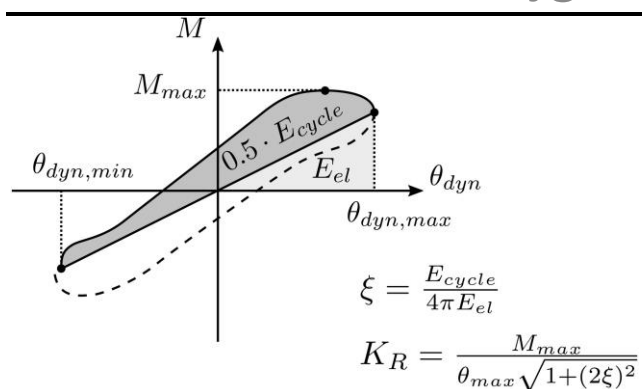


Fig. 7.



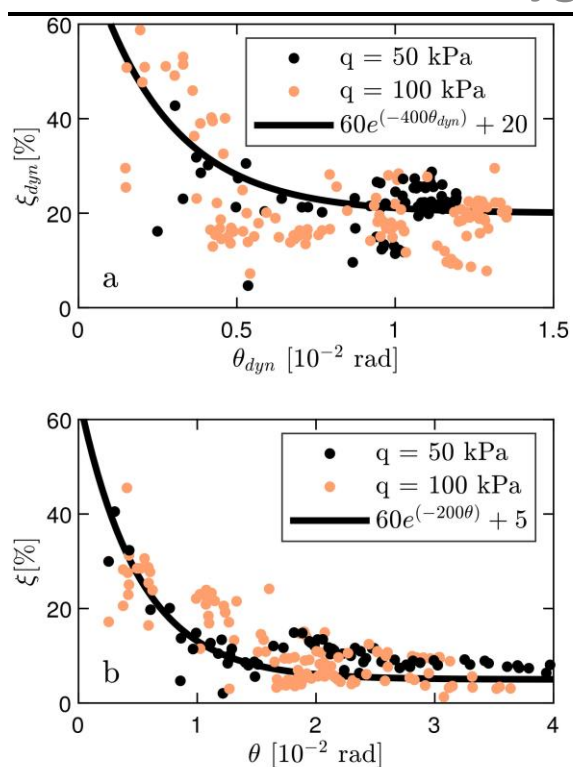


Fig. 8.

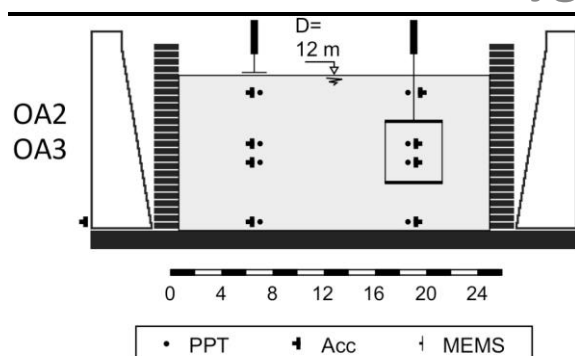
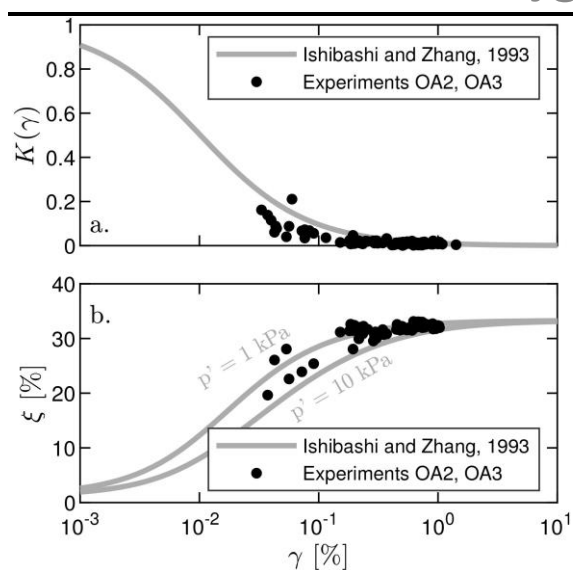


Fig. 9.



**Fig. 10.**

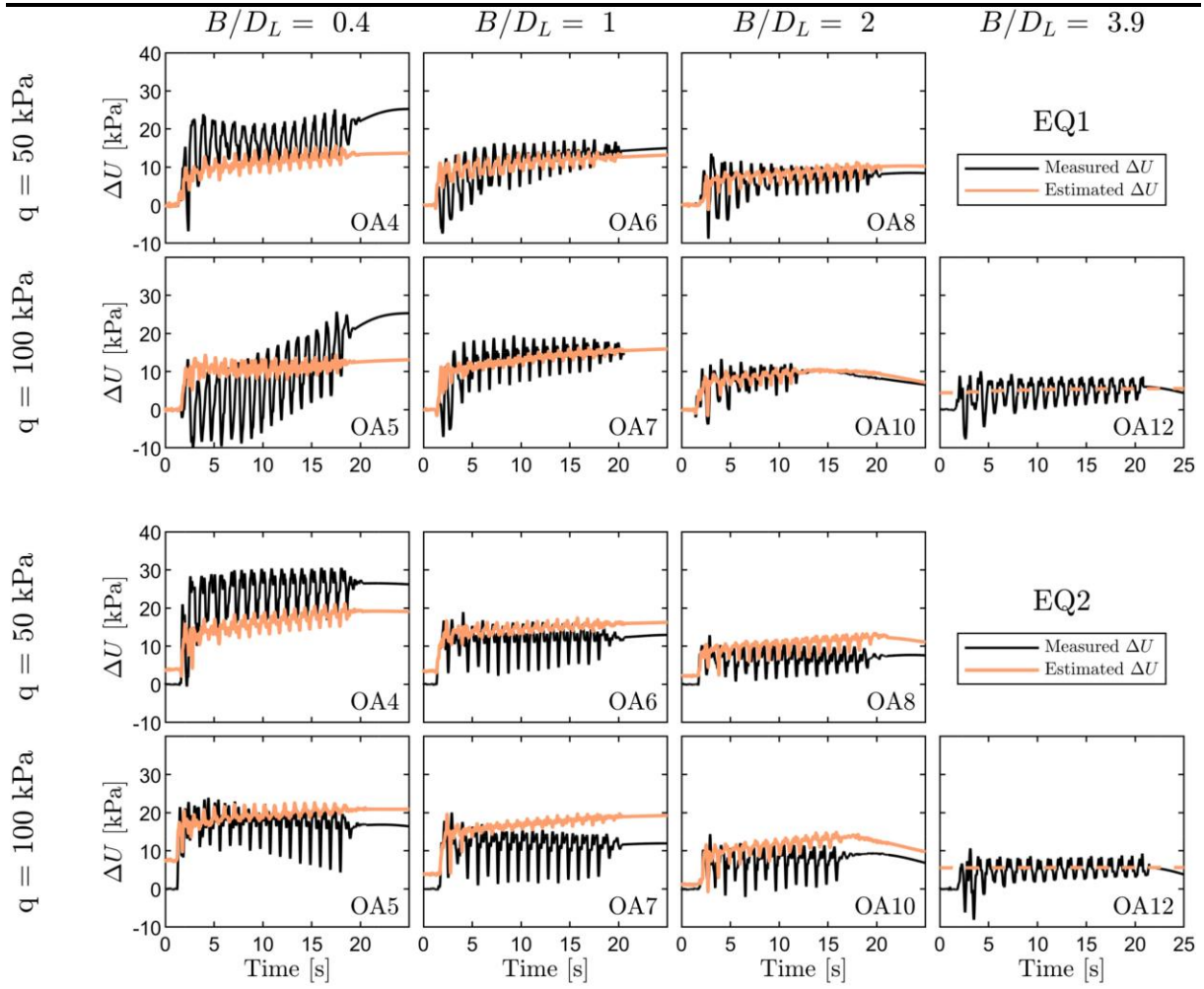
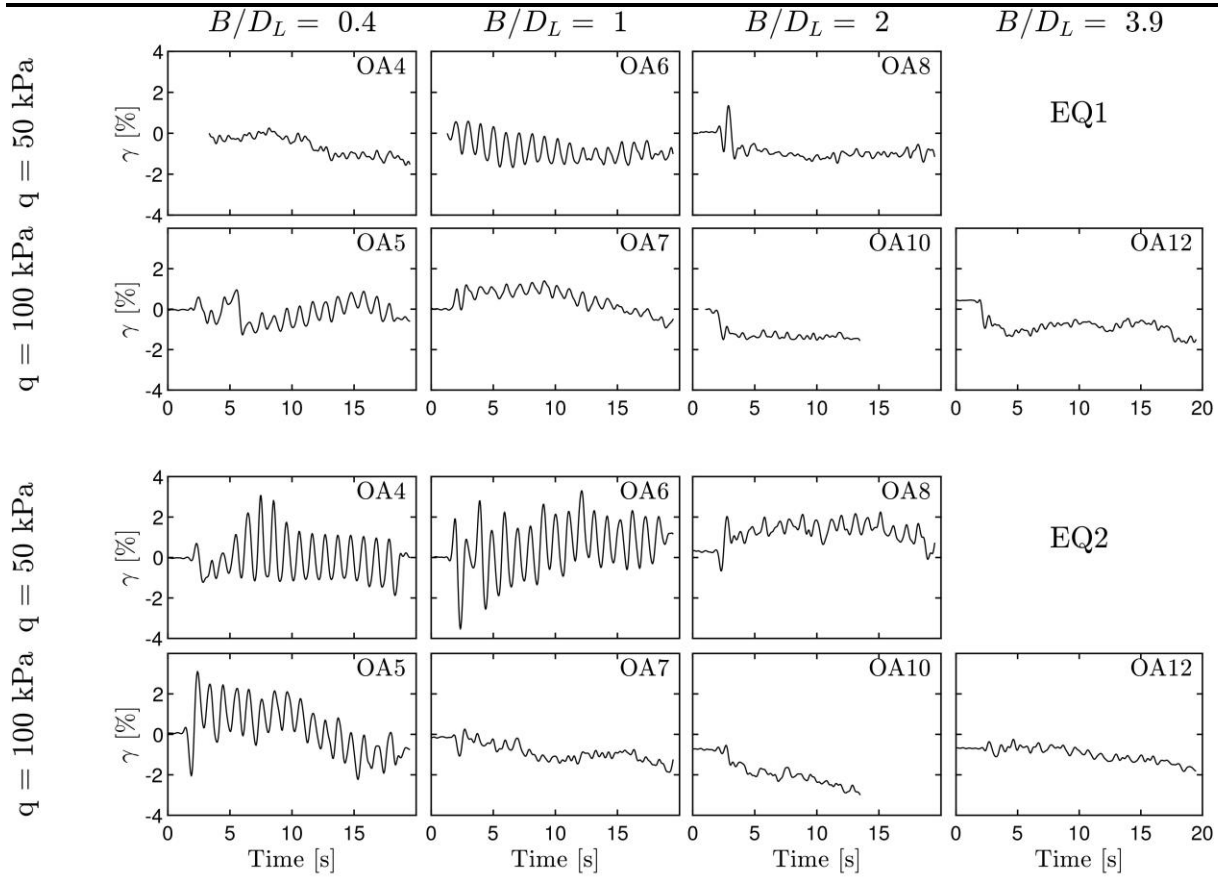


Fig. 11.



**Fig. 12.**

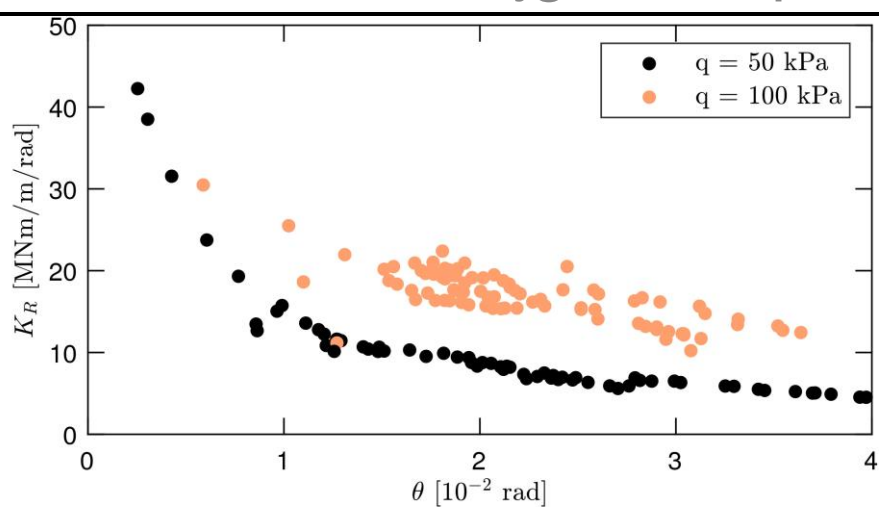


Fig. 13.

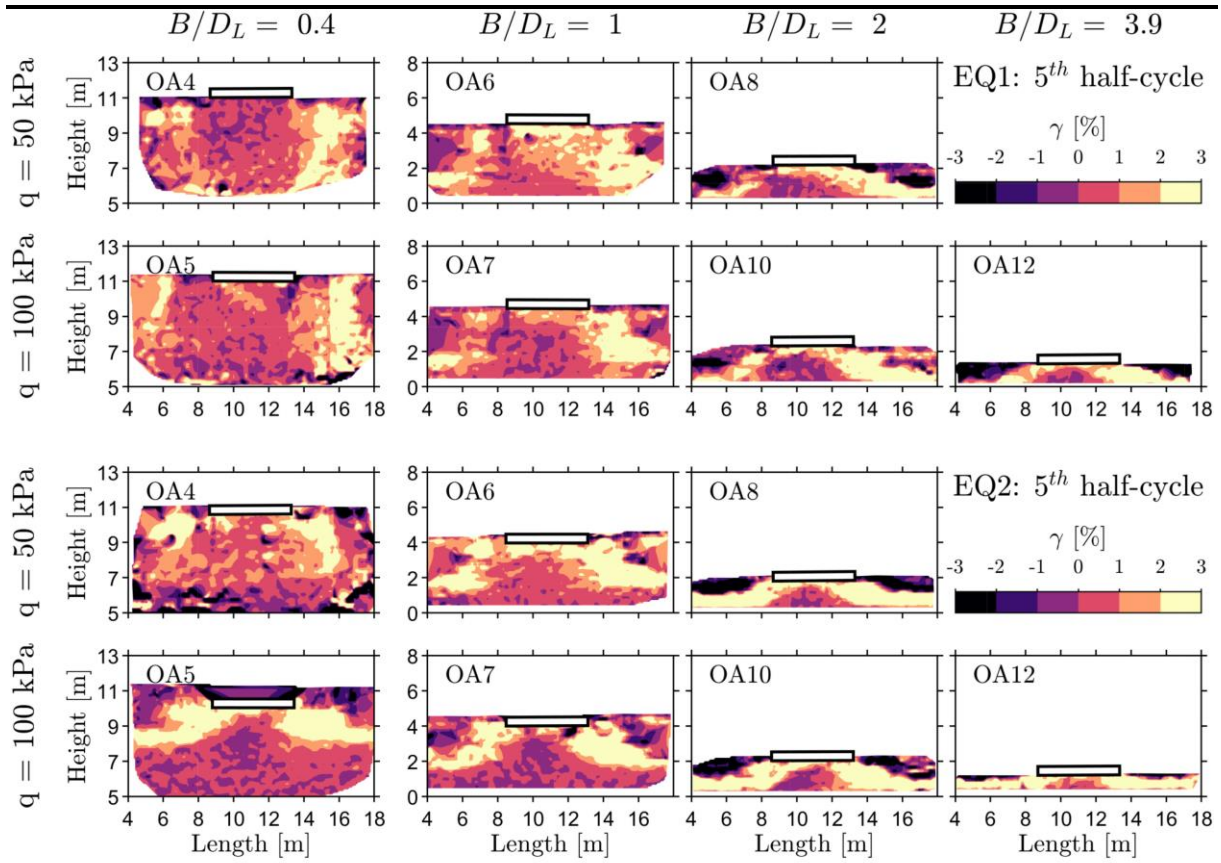


Fig. 14.

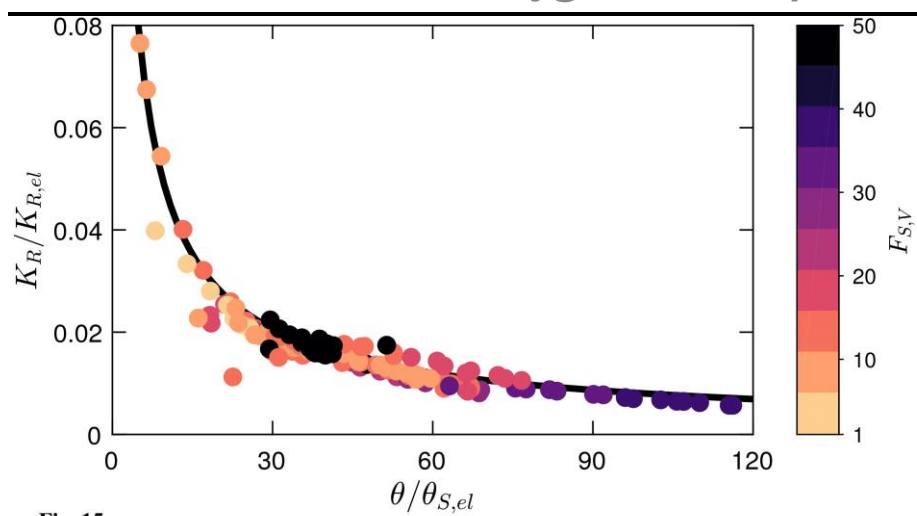


Fig. 15.



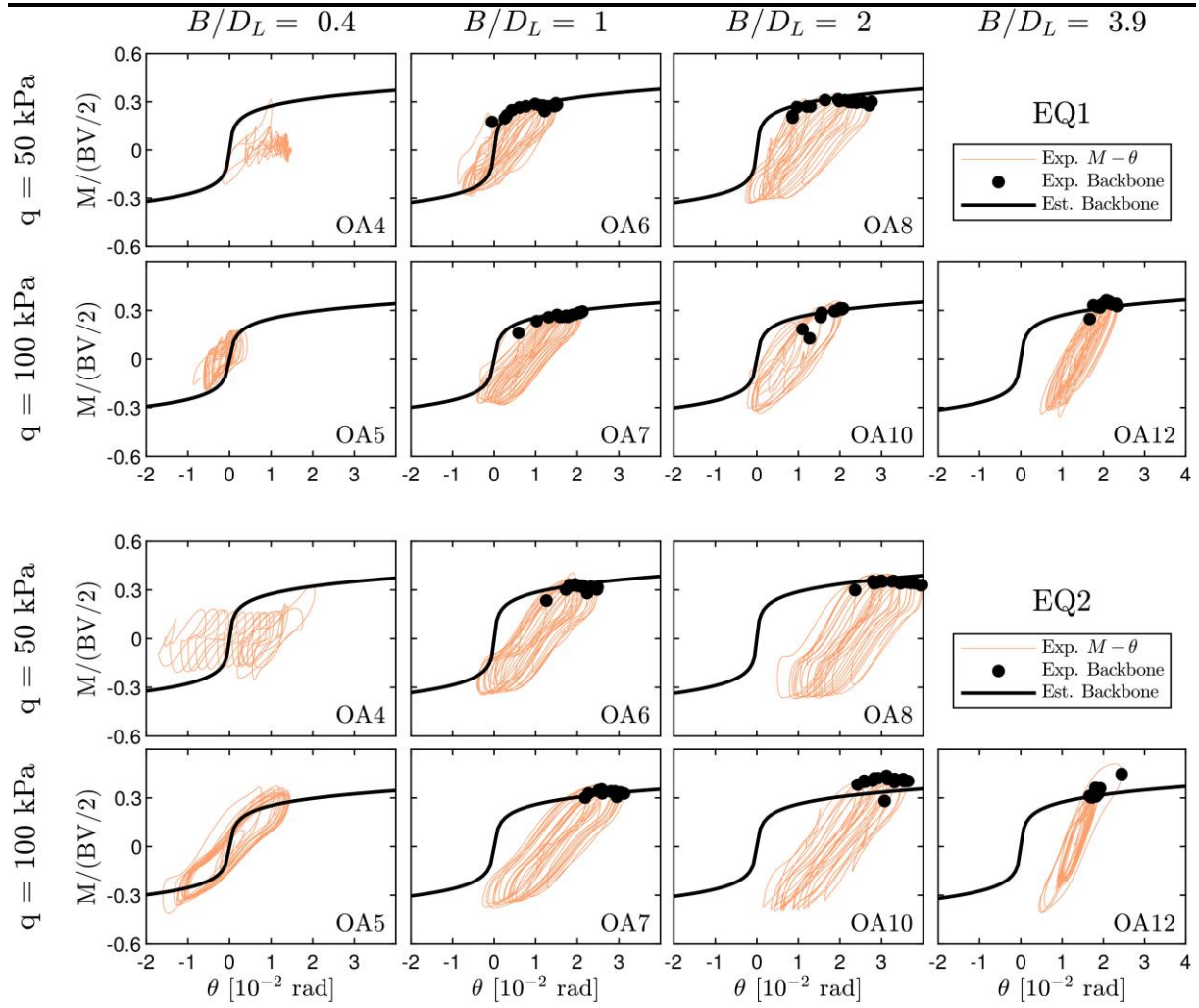
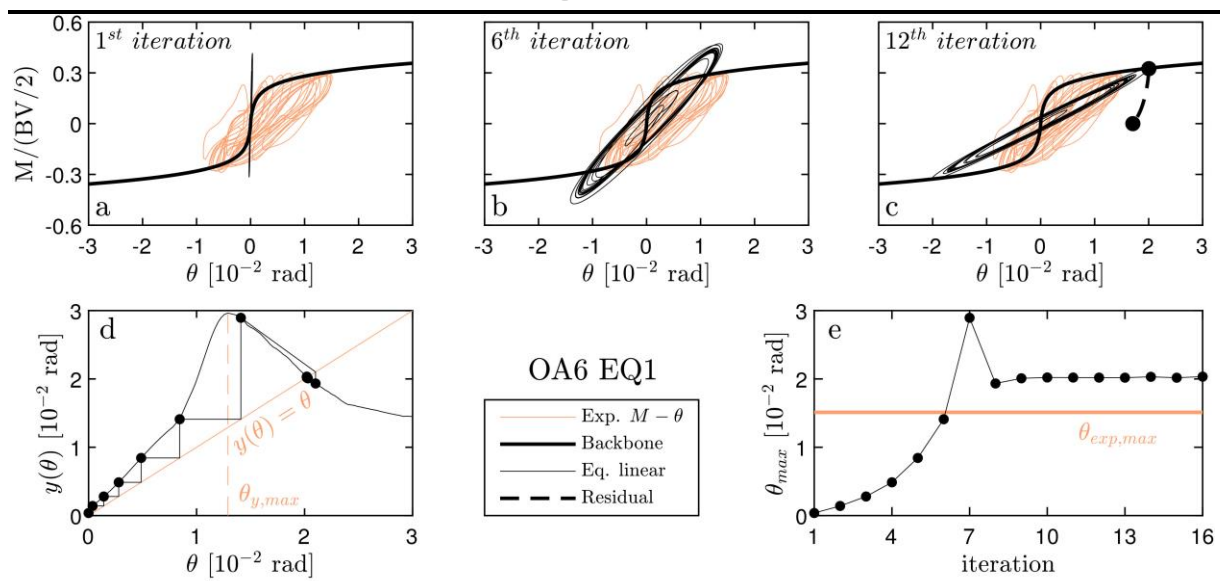
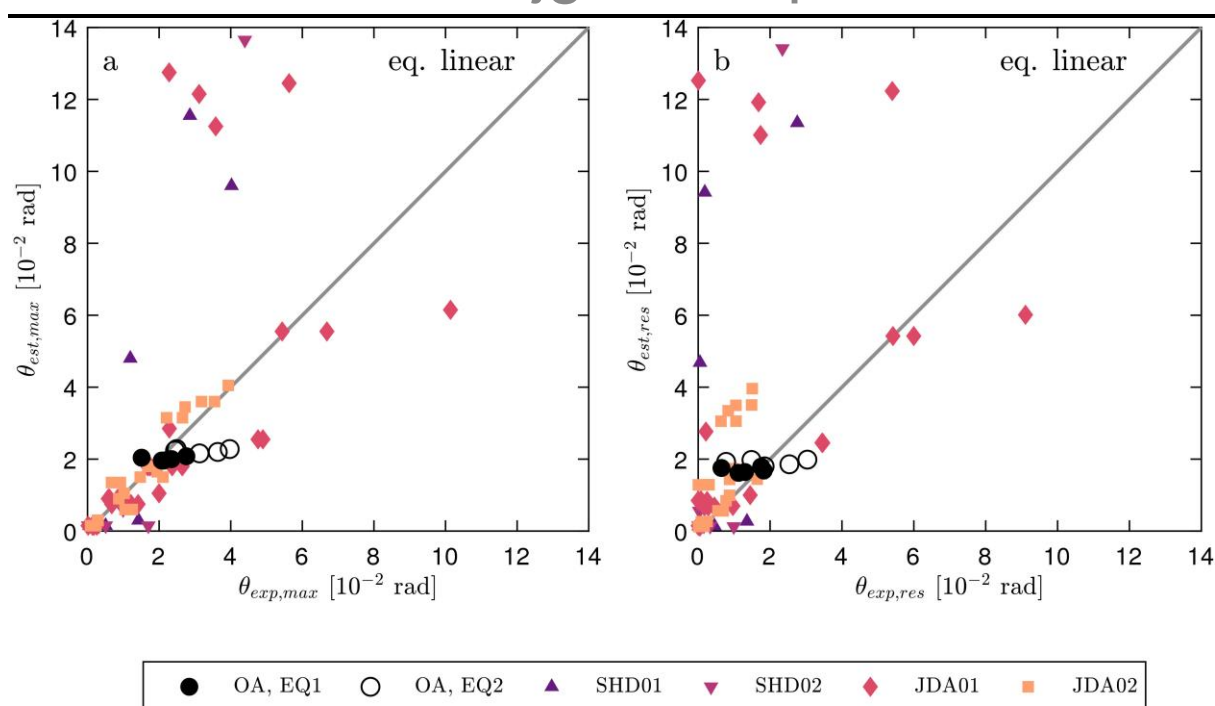


Fig. 16.



**Fig. 17.**



**Fig. 18.**

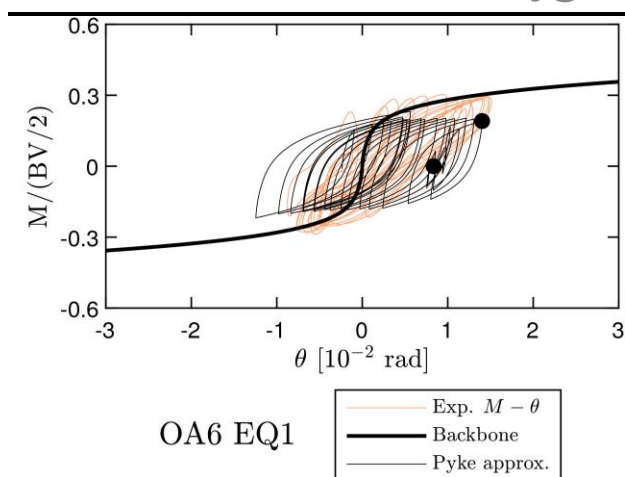


Fig. 19.

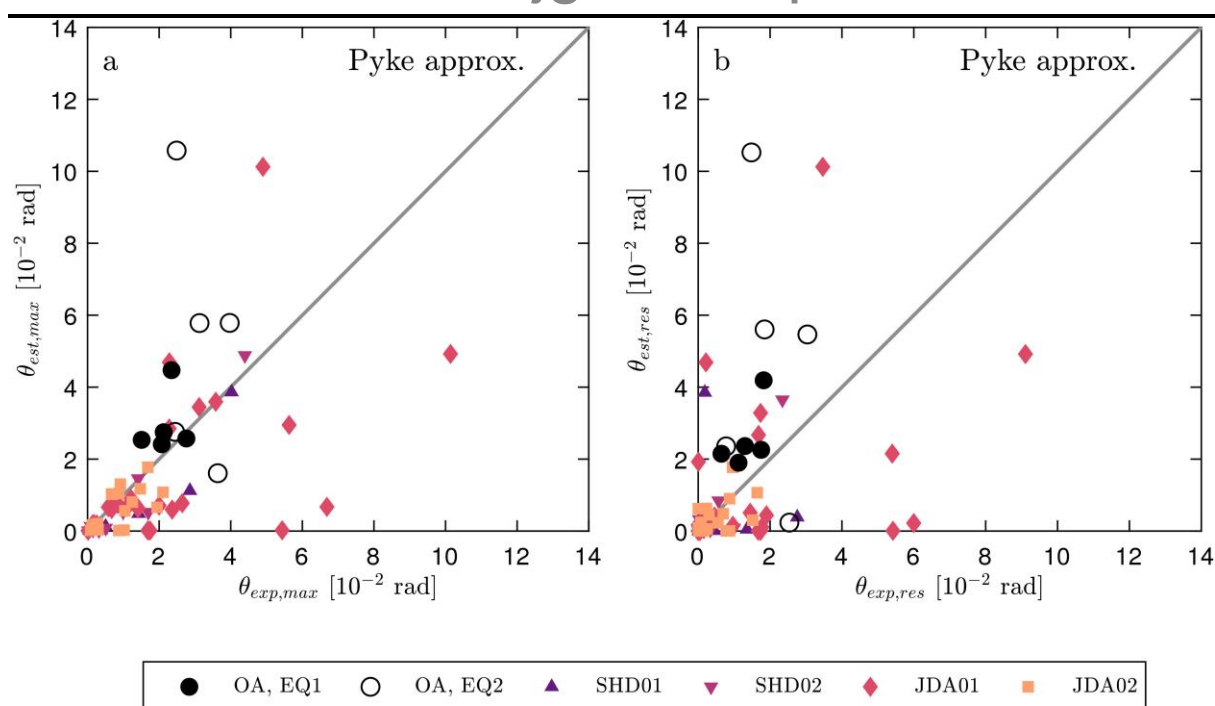


Fig. 20.